Mixing Efficiencies in Turbulent Tidal Fronts: Results from Direct and Indirect Measurements of Density Flux

ANN E. GARGETT

Institute of Ocean Sciences, Sidney, British Columbia, Canada

J. N. MOUM

College of Oceanic and Atmospheric Sciences, Oregon State University, Corvallis, Oregon

(Manuscript received 9 September 1994, in final form 27 January 1995)

ABSTRACT

The authors report direct measurements of density flux at a single depth in a turbulent tidal flow, made by towing a CTD beside the vertical beam of a modified acoustic Doppler current profiler. The direct flux estimates are compared with indirect estimates of density flux based on simultaneous microscale profiler measurements of ϵ and χ, dissipation rates of turbulent kinetic energy and of temperature variance, respectively. Two mixing efficiency estimates are made using Γ_d from the ratios of indirect flux estimates and Γ_o from the ratio of direct to ϵ flux estimates. The analysis indicates that

- Γ_d is no different from that determined in other open ocean experiments and is independent of the sign of the flux
- $\Gamma_d < |\Gamma_o|$, regardless of the sign of the flux
- Γ_o (flux > 0) $< |\Gamma_o|$ (flux < 0).

The consequences for interpretation of ocean microstructure flux estimates are discussed.

1. Introduction

The presence of turbulence in a fluid system is accompanied by rates of dissipation and diffusion that are many times molecular. Because both stratification and rotation tend to inhibit vertical transfer in the ocean, the enhancement of vertical fluxes of density and other water properties is perhaps *the* property of turbulent flows that has the most profound implications for a wide variety of oceanic problems, from practical (appropriate locations for marine dump sites or fish farms) to fundamental (nutrient resupply to euphotic zones, mechanism and stability of the thermohaline circulation). Unfortunately, direct measurements of turbulent fluxes, as an average value of the product of fluctuation scalar (such as density) and vertical velocity w, are extremely difficult to make in the ocean. The measurement of w is very easily contaminated by vehicle motion, while the turbulent part of the w field is often smaller than that associated with internal waves in the stratified interior of the deep ocean. Consequently, there are only a few published reports of attempts at direct flux measurement: Yamazaki and Osborn (1993) report determinations of density flux from a shear layer sampled by submarine; Fleury and Lueck (1994) made estimates from high-pass filtered values measured on a towed body; Moum (1990) presented values measured on repeated passes of a profiler free-falling vertically through a turbulent "patch."

Present values for K_ρ, the turbulent vertical diffusivity of density used to parameterize the turbulence-induced flux of density in the ocean interior, are based rather upon a much larger (though still probably inadequate) set of indirect estimates of turbulent fluxes, made by measuring a dissipation rate and subsequently applying one of two commonly used models. The model of Osborn (1980) uses $\langle\epsilon\rangle$, the average rate of dissipation of turbulent kinetic energy per unit mass, to estimate density flux from a simplified steady-state balance of turbulent kinetic energy (TKE)

$$-\langle u'w'\rangle U_z = \langle\epsilon\rangle + g\rho_0^{-1}\langle\rho'w'\rangle,$$

which yields

$$F = \langle\rho'w'\rangle = \Gamma_o\rho_0 g^{-1}\langle\epsilon\rangle = \Gamma_o F_\epsilon, \qquad (1)$$

where $F_\epsilon \equiv \rho_0 g^{-1}\langle\epsilon\rangle$, angle brackets denote some suitable averaging to eliminate divergence terms, and $\Gamma_o = R_f/(1 - R_f)$ is related to the flux Richardson number

Corresponding author address: Dr. Ann E. Gargett, Institute of Ocean Sciences, P.O. Box 6000, Sidney, BC V8L 4B2, Canada.
E-mail: anng@ios.bc.ca

$$R_f \equiv \frac{-g\rho_0^{-1}\langle\rho'w'\rangle}{\langle u'w'\rangle U_z} = \frac{\Gamma_o}{(1+\Gamma_o)},$$

the ratio of buoyancy sink to shear source terms in the TKE equation. A final assumption is that the "efficiency" of turbulence in working against the gravitational field to produce vertical density flux is relatively low—that is, $R_f \ll 1$ (Stewart 1959): thus the flux coefficient $\Gamma_o \ll 1$, a value of ~ 0.2 being a common choice, based upon laboratory measurements of R_f (Linden 1972; Rohr and Van Atta 1987).

The second model, that of Osborn and Cox (1972), assumes a particular balance of terms in a steady-state equation for fluctuation temperature in order to use dissipation rate of mean-square fluctuation temperature $\langle\chi\rangle = 2D_T\langle(\nabla T')^2\rangle$, where D_T is molecular diffusivity of temperature, to estimate an eddy diffusivity for temperature as

$$K_T \equiv -\langle w'T'\rangle T_z^{-1} = 0.5\langle\chi\rangle T_z^{-2},$$

where T_z is the mean vertical gradient of temperature. Assuming that oceanic density is nearly linear in T and S, density flux can be written as $\langle\rho'w'\rangle = -K_\rho\rho_z$, where ρ_z is the mean vertical gradient of density. If finally it is assumed that T and S are mixed equally efficiently by turbulence, $K_\rho = K_T$ and hence

$$\langle\rho'w'\rangle = -0.5\langle\chi\rangle T_z^{-2}\rho_z \equiv F_\chi. \qquad (2)$$

When both ϵ and χ are measured simultaneously, Eqs. (1) and (2) lead to an observationally determined estimate of Γ_o, a dissipation flux coefficient

$$\Gamma_d = \frac{F_\chi}{F_\epsilon} = \frac{\langle\chi\rangle N^2}{2\langle\epsilon\rangle T_z^2}, \qquad (3)$$

where $N^2 = -g\rho_0^{-1}\rho_z$ is the buoyancy frequency, and the subscript reminds us that this is an estimate derived from dissipation-scale quantities. Such datasets are not numerous, mainly because successful measurements of ϵ and χ with existing sensors require conflicting vehicle characteristics, faster mean speeds for ϵ measured by airfoil probes, slower mean speeds for χ measured by thermistors. However, existing datasets from double-diffusively stable regimes yield values of Γ_d in the range 0.1–0.4 (Oakey 1985; Gregg et al. 1986; Peters et al. 1988; Moum et al. 1989). We will use the term "dissipation method" to describe the use of Eq. (1), with Γ_d in place of Γ_o to predict density flux.

Over the past five years, development of a modified acoustic Doppler current profiler [the *DO*ppler *T*urbulence (DOT) system, Gargett 1994] has enabled measurement of the energy-containing scales of the vertical velocity field associated with tidally generated turbulence in British Columbian coastal waters. Addition of a CTD towed at constant depth very near (although not within) the vertical acoustic beam offered the possibility of direct flux determination using what the atmospheric boundary layer community terms the eddy-correlation technique, that is, direct average of the product $\rho'w'$. Simultaneous profiling for ϵ and χ could then test the indirect methods (1) and (2), which form the basis for the present assessment of turbulent mixing in the ocean. This paper reports such measurements and comparisons, carried out at a single depth, on transects through turbulent tidal fronts that form in consistent locations in tidal channels between southern Vancouver Island and the British Columbia/Washington mainland coast. Whereas the associated turbulence is considerably more intense than that typical of the ocean interior, the local water column stratification (against which the turbulence must work to produce vertical density flux) is also much larger than deep-ocean stratification, suggesting that the present results may be applicable to a broader range of flows.

2. Observational background

Figure 1 is a map of the tidal channel complex in which measurements were taken during a two week period in July 1992. Haro Strait and Boundary Pass form the major deep water channel connecting Juan de Fuca Strait (bordering southern Vancouver Island to the SW of this area) and the Strait of Georgia (to the NW). On all but the weakest ebb tides, tidal fronts typically form near the positions denoted by wavy lines: we will refer to these as 1) the Moresby front, 2) the Turn Point front, and 3) the Stuart Island front. These fronts are quite different from shallow sea tidal fronts, first described by Simpson and Hunter (1974), which form as boundaries of regions where turbulence generated by tidal flow is strong enough to eliminate water column stratification. Water column stratification is changed but not eliminated by the fronts in British Columbian coastal waters, which appear to form instead in positions of horizontal convergence of the mean tidal flows, associated with abrupt changes in channel shape and/or direction. The fronts are certainly strongly convergent at the surface, with flotsam quickly accumulating to mark frontal boundaries. The first Doppler measurements in these fronts (Gargett 1988), made from a drifting ship, showed predominantly downward vertical velocities as the ship drifted into and along this strong frontal convergence. The magnitude of the associated dissipation values (if not the boils and vortices obvious on the water surface!) made it clear that turbulence in such fronts plays a major role in the transformation of water properties, which occurs during the flow of water between the Strait of Georgia and the continental shelf off the mouth of Juan de Fuca Strait (Griffin and LeBlond 1990; Crawford 1991; Farmer et al. 1994). It was also clear, however, that any attempt to make acceptable measurements of turbulent properties associated with the tidal fronts would have to be taken in a way that avoided the bias inherent in Lagrangian measurements in the presence of strong convergences. Our measurements were taken from a

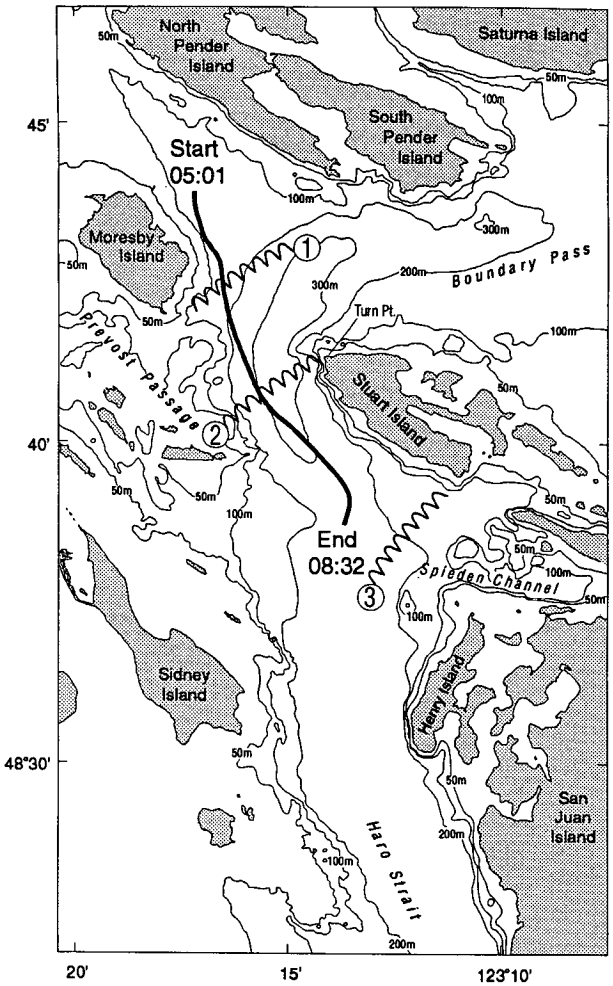

FIG. 1. Map of the tidal channel complex in which measurements were taken: Haro Strait and Boundary Pass are the major deep water channels connecting Juan de Fuca Strait (SW) to the Strait of Georgia (NW). Convergent tidal fronts typically form on most ebb tides around the positions sketched: 1) Moresby front, 2) Turn Point front, and 3) Stuart Island front. The heavy line is the ship track during a typical measurement run (run 1), taking 2–3 hours in a region where the dominant tidal forcing is semidiurnal.

ship moving (approximately) with the mean tidal flow, at an average speed of $V_g = 1$ m s^{-1} through the water, the maximum speed that did not cause excessive vibration in the Doppler side-mounting strut. Depending on the tidal flow, speed over the ground varied within the range 1–2 m s^{-1}. Since the local tide is predominantly semidiurnal, and a typical run (heavy line in Fig. 1) took approximately 2–3 hours, it was often possible to make two runs on each ebb.

The suite of instruments deployed on each run is shown in Fig. 2. The vertical acoustic beam of the DOT system (B3) provided estimates of w every 2 s. These were binned every 2.31 m beginning at depth 6.11 m. The CTD was deployed immediately above a streamlined weight designed to keep the CTD sensors aligned into the flow: due to physical restriction of the forward tow point, depth of tow was usually in the range d = 20–30 m. With the ship underway at the desired speed, the tow point was adjusted to place the CTD approximately 1 m forward and outboard of B3. Adjustment was done by moving the tow position toward the stern until the CTD/tow weight became just visible as an acoustic reflector in A3, the amplitude field of B3, then moving it forward until the amplitude signal disappeared. The position of the tow was monitored throughout the runs, both visually and via A3, and the tow point was manually adjusted when large changes in relative flow moved the CTD more than about 1 m from its initial position. Such adjustment, interrupting the continuous measurement of density necessary for flux calculations, was fortunately rarely needed. The freefall microscale profiler Chameleon was deployed repeatedly through the CTD tow depth to a maximum depth of ~50 m, and recovered to the stern of the ship (approximately 4 m aft of the DOT transducer) between profiles. The maximum profile depth was chosen to allow resolution of "mean" water property gradients by vertical reordering (Thorpe 1977), while obtaining as many realizations as possible through the range of the CTD tow depth. Operated at an average fall speed of ~1 m s^{-1} to 50 m, profiles were made at a rate of

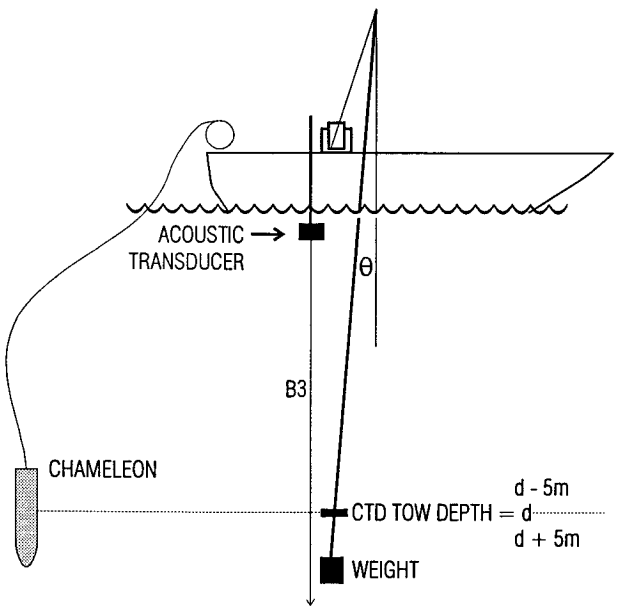

FIG. 2. Instrument configuration for simultaneous towed and dropped measurements of buoyancy flux. A CTD was towed at depth d, with tow point adjusted to place the CTD approximately 1 m forward and outboard of the vertical beam (B3) of a modified acoustic Doppler current profiler (Gargett 1994). The microstructure profiler, Chameleon, was deployed repeatedly through the CTD tow depth, recovering to the stern of the ship between profiles. Profiler dissipation rates within $d \pm 5$ m were used to form indirect estimates of buoyancy flux for comparison with flux values computed from fluctuation w and ρ measured by the Doppler and CTD, respectively.

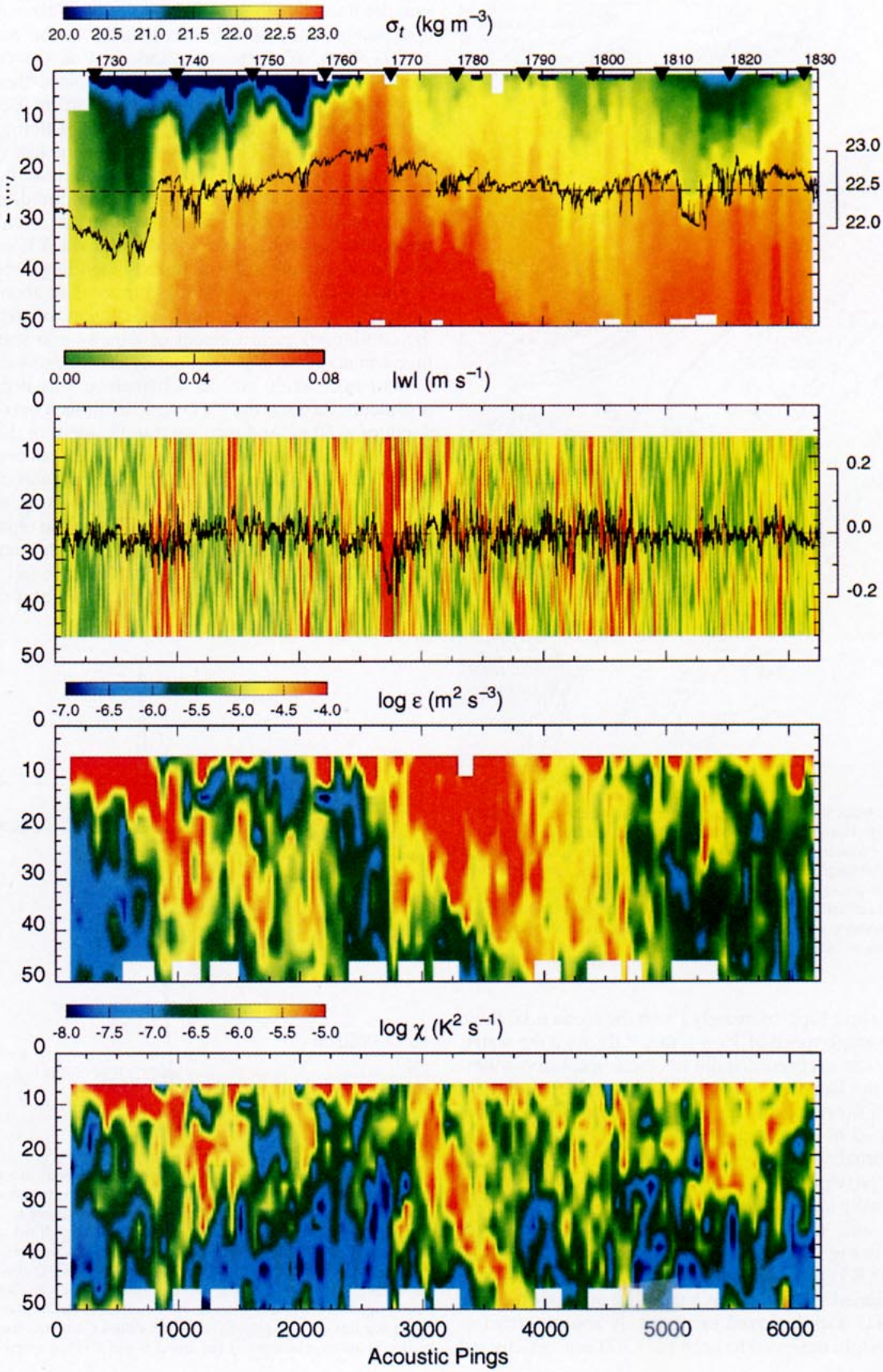
20.0 20.5 21.0 21.5 22.0 22.5 23.0
σt (kg m−3)
1730 1740 1750 1760 1770 1780 1790 1800 1810 1820 1830
0 10 20 30 40 50
z (m)
23.0
22.5
22.0
0.00 0.04 0.08
|w| (m s−1)
0.2
0.0
-0.2
-7.0 -6.5 -6.0 -5.5 -5.0 -4.5 -4.0
log ε (m2 s−3)
-8.0 -7.5 -7.0 -6.5 -6.0 -5.5 -5.0
log χ (K2 s−1)
0 1000 2000 3000 4000 5000 6000
Acoustic Pings

about 30–35 per hour. Dissipation rates calculated from profiler variables within $d \pm 5$ m were used to form the buoyancy flux estimates (1) and (2) for comparison with flux values computed from fluctuation w and ρ measured by the Doppler and CTD, respectively.

Although vertical velocity fluctuation measurements were made from Chameleon using a pitot tube (Moum 1990), dropped flux estimates were not made for this dataset because the vertical scales of the flux-containing eddies (tens of meters; Fig. 7a) are much larger than the profiler and we do not expect the profiler measurements to resolve these scales. Note, however, that this flow regime is an extreme example. Estimates from the main thermocline, where we expect the flux-containing scales to be much smaller, have no such limitation (Moum 1994).

Figure 3 depicts the kind of data obtained during a typical run (run 1, shown in Fig. 1). All fields are shown relative to the Doppler ping number (recorded for the profiler at the time of release), since in subsequent analysis of the towed fields this is directly interpretable as number of measurements: for equivalent time in seconds, multiply by 2. Fields of (a) σ_t and the logarithms of (c) ϵ and (d) χ are contoured from 105 vertical profiles, and clearly denote the changes in density and the increases in ϵ and χ, which are associated with the Moresby front ($\sim$ ping 750) and the Turn Point front ($\sim$ ping 2750). Density stratification is double-diffusively stable, with warm, fresh surface waters overlying colder saltier deep water, and is predominantly due to salinity. Density from the CTD tow, superimposed on panel (a) at the depth of measurement, shows the details of the large-scale changes seen in the contoured profiler field. The CTD sample period is 2 s, rather than the approximately 2 min between microscale profiles; hence, the CTD time series contains higher-frequency fluctuations associated with the flux-carrying eddies. The w field, also sampled every 2 s, is difficult to contour on this scale; panel (b) contains not 105 but over 6000 profiles, with consequent increase in complexity. In addition, it has been necessary to color code the absolute value of w, so that sign must be determined with the help of the superimposed time series of w from the depth bin containing the CTD tow depth. However, this illustration emphasizes the range of scales involved in the measured flows, as well as their complexity and space/time inhomogeneity.

Further details of the measured variables and associated flux computations are found in section 3 for the towed flux estimates and section 4 for the dropped flux estimates; section 5 presents results based on the entire dataset. These results and their possible implications for interpretation of oceanic microstructure measurements are discussed in section 6.

3. Towed flux measurements

a. Measurement of w

The DOT system has been described in some detail by Gargett (1994); only those features important to the present application are repeated here. The measurement of w was made with one beam of a modified 600-kHz transducer, aligned carefully to the vertical at the beginning of every run. With vertical bin length of 2.31 m, transducer face at 3.8 m, and blank-after-transmit of one bin, the top of the first measurement bin was 6.11 m. For the chosen setup, the Doppler speed measurement in bin i represents a (half-overlapped) triangular spatial average over 4.62 m, centered at $d_i = (6.11 - 1.11)$ m $+ i \times 2.31$ m, where the -1.11 m is a correction for lag associated with a low-pass filter in the Doppler processing circuit (Chereskin and Harding 1993). "Raw" speed estimates were made as ensemble averages over four 0.5 s pings. The "percent good" variable was set to flag an ensemble as "bad" if more than one of the four pings failed the manufacturer's signal-to-noise criterion: such "bad" ensembles, in practice both rare and isolated, were easily edited out of the dataset before further processing. With an average ship speed of 1 m s^{-1} over ground, the sample period of 2 s in time converts to 2 m of horizontal distance, and the two have been used interchangeably here.

The "raw" speed estimates had noise standard deviation of 0.0525 m s^{-1}, determined from runs at slack water in a protected coastal inlet (Gargett 1994). This was reduced to 0.011 m s^{-1} by repeated smoothing in both time (horizontal) and vertical dimensions: the resulting noise spectra were white at low wavenumber, with 3 dB point corresponding to approximately 13 m in both horizontal and vertical.

b. Measurement of density

The towed CTD was an Ocean Sensors Model 200, set and calibrated for increased resolution in T and S: density was calculated from measured T, S, and p, referenced to zero pressure since the tow was shallow.

FIG. 3. Run 1: color-contoured fields of (a) σ_t, (c) logϵ, and (d) logχ from the Chameleon profiler (105 profiles at about 2-minute intervals: profile numbers shown for every tenth profile along the top border of the upper panel). Shown superimposed on panel (a) at tow depth, the density record from the towed CTD (sampled every 2 s) shows the same large-scale structure and, as well, smaller structures associated with the density flux. Mean tidal flow is in the direction of measurement, from left to right. The run crosses two tidal fronts, around pings 750 and 2750 (ping axis on bottom panel). Horizontal convergence in the fronts generates large vertical velocities, contoured as absolute value in panel (b), which are associated with enhanced levels of ϵ and χ. The superimposed time series of w at the depth of the CTD tow allows determination of the local sign of the w field.

Because horizontal gradients are less sharp than vertical ones, and because the spatial response of the conductivity sensor closely matches that of the thermistor used for temperature at our mean tow speed of 1 m s^{-1}, "spiking" in calculated salinity is undetectable in the tow records. A typical tow record of p, T, S, and σ_t (density (kg m^{-3})-1000) is shown in Fig. 4 (run 1, as in Figs. 1, 3). The pressure record shows the stability of depth within a tow, as well as the location of reference points (1–3) needed to check time alignment of the CTD and the Doppler time series, crucial to flux measurement. The DOT acquisition system runs under a computer clock, while the CTD has an internal clock, initially set from the clock of a second computer. Although both computer clocks were reset before every run, there is the possibility of time offsets due to inaccurate relative reset values and/or to times involved in writing header information in the Doppler program. To ensure time alignment, at the end of every run we noted the DOT ping numbers associated with a sequence of changes in CTD depth: 1) move down 5 m from the tow depth, 2) move up 10 m from there, and 3) return to the surface. The time stamps of the DOT pings and the associated CTD records (clearly identifiable in the pressure signal) allow calculation of a time offset correction.

It is difficult to set the CTD to a specific sample period—that is, to match exactly the DOT 2-s sample period. Thus, the CTD sample period used (1.98 s) was somewhat shorter than that of DOT, allowing the CTD data to be linearly interpolated to the DOT 2-s sample period. Finally the "raw" density time series is passed through the same filter procedure used to reduce the noise variance of the raw Doppler data, producing the same resolution in time (horizontal distance) while maintaining relative phase, also crucial to flux measurement.

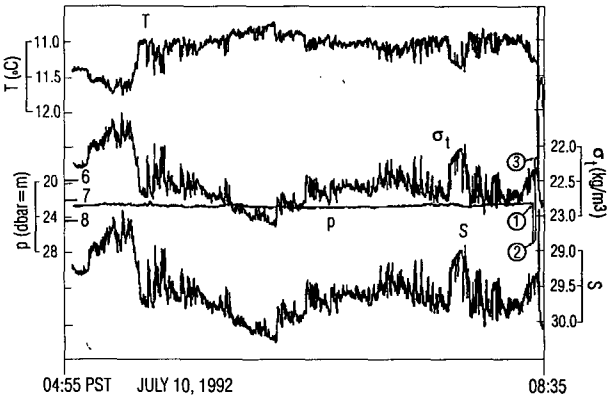

FIG. 4. Typical record (run 1) of pressure (p), temperature (T), salinity (S), and density (σ_t) obtained from a CTD tow. The pressure record shows the stability of depth within a tow, as well as the location of reference points (1–3) used to check time alignment of the CTD and the Doppler time series. The depths marked are those associated with DOT velocity bins 6, 7, and 8.

The three sets of simultaneous measurements of w and σ_t shown in Fig. 5 provide a more detailed look at the range of data available (and will be used as examples in discussion of the towed flux estimates). The middle time series in each is the σ_t time series after (phase preserving) high-pass filtering [see discussion in subsection 3c(1)]. Panel (a) shows the long run 1 seen before in Figs. 3, 4: Fig. 5b is an enlargement of a section of this record (comparable in length to the other two records shown) in which the towed density flux estimate is significant and positive (downgradient). Figure 5c is a record in which the singular nature of the large density feature around ping 400 makes the local density flux estimates unreliable: the latter part of this record has significant negative (countergradient, restratifying) density flux. Figure 5d depicts a record in which towed flux estimates are not significantly different from zero, although the w and ρ fluctuations are above instrumental noise levels.

c. *Concerns about meaningful flux calculations from DOT/CTD system*

There are four major features of the physical system being measured, as well as the means by which the measurements are taken, that influence the reliability of flux calculations.

1) LARGE-SCALE STRUCTURE OF THE DENSITY FIELD AND THE NEED FOR FILTERING

Over long tow records, the density field at constant depth often shows a trend associated with general progression toward fresher (saltier) water when the tow is away from (toward) the open ocean. In addition to a trend, the density record often contains relatively abrupt changes (see examples marked * in Fig. 5a) at frontal boundaries. While it seems clear that the overall trend in density should be removed before calculating fluxes, it is less obvious whether to consider the frontal water mass changes as part of the flux signal, or as a "background" of mesoscale water masses which would remain if the turbulent velocity structure were to decay away. We tend to the latter view; however choice of appropriate cutoff frequency for high-pass filtering density requires careful examination of the scales responsible for carrying the flux.

2) SPATIAL INHOMOGENEITY AND THE NEED FOR LOCAL FLUX ESTIMATES

A major feature of tidally induced turbulence in coastal waters is its spatial inhomogeneity. The tidal fronts in which the present measurements were made are associated with channel geometry. The vertical velocity signal typically rises abruptly as a front is crossed, then decreases gradually downstream, unless another front is encountered. As illustrated by Figs. 3c and 3d, the associated dissipation fields are also highly

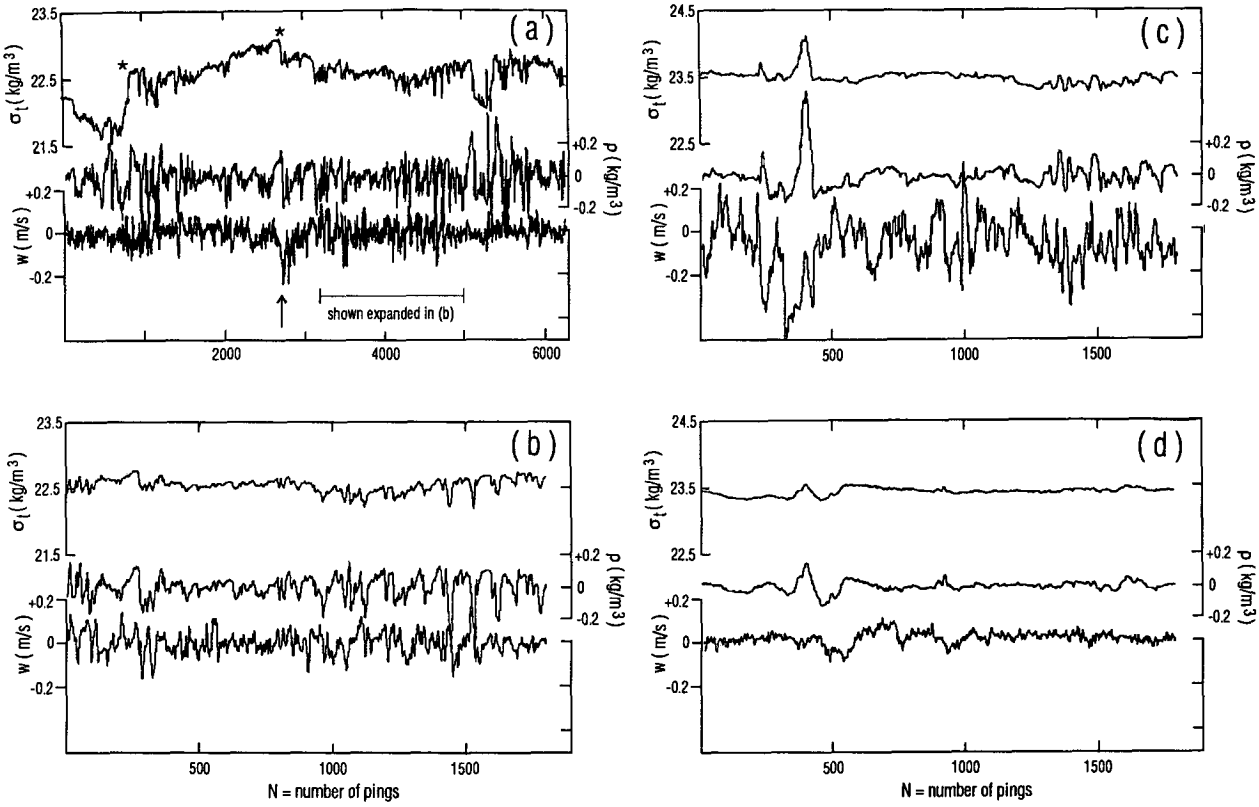

FIG. 5. Records of σ_t and w (upper and lower traces, respectively) vs number of pings N (approximate horizontal distance L (m) = $2N$): the center trace in each panel is ρ = sigmat after high-pass filtering with phase preservation. Scales of σ_t, ρ, and w are the same in all panels, to emphasize the variety of observed signal levels. (a) Run 1: a long continuous run during neap tides; stars indicate positions of tidal fronts. Panel (b) is an enlargement of the marked portion, on the same horizontal scale as (c) and (d). (c) Run 2: a spring tide record with much larger w fluctuations; isolated density anomalies like that at $N \sim 400$ prevent meaningful flux estimates. (d) Run 3: w levels are low but remain above noise.

inhomogeneous. The strong spatial inhomogeneity of the field precludes making a single flux estimate over an entire towing record. Thus, we must decide how to segment the record for flux calculations.

3) THE PROBLEM OF SAMPLING STRONGLY CONVERGENT FLOWS

Another problem arises because of the tendency of the strong horizontal surface convergence characteristic of the tidal fronts to sweep up surface objects, including slowly moving ships! In the strongest fronts, surface velocities are comparable to mean ship speed and tend to force the ship into the front, where the Doppler measures the strong downward vertical velocity fed by the horizontal convergence (cf. Fig. 5, arrows). The necessary mass continuity is achieved by upwelling events: however, because these are associated with horizontal *divergence,* the ship tends to be forced away from such regions, hence measures a preponderance of downward mass flux. Although the moving-ship measurements are less biased than measurements from a truly Lagrangian platform, we still need a means of identifying and flagging records where the ship is trapped in a front.

4) CHANGES IN HORIZONTAL POSITION OF THE CTD

The angle of the CTD towing cable to the vertical could vary as fluctuating horizontal velocities caused varying drag on the cable, CTD, and weight. Most major variations arose when ship speed had to be increased to free the ship from a strong convergence. The position of the tow cable was continuously monitored, and the CTD tow position manually adjusted whenever it moved more than 1 m from the optimal tow position, chosen to place the CTD near but not within the vertical beam. Because of the way in which the tow was rigged, such adjustments are clearly visible as sharp changes in the tow depth, and the tow records have been segmented around these occasions, fortunately fairly rare. However, there was no way to monitor small variations in tow angle, hence horizontal position. Even though it is expected that random variations in phase due to vary-

ing position would only decrease coherence, hence flux estimates, it would be desirable to assess the effect horizontal position changes of order 1–2 m could have on calculated flux values.

Before documenting the method used for towed flux calculation, pointing out how the above difficulties have been addressed and/or quantified, we first explore the nature of the measurements of σ_t and w obtained in the tidal fronts.

d. Spectra and cospectra

Classical spectral techniques, requiring that many wavelengths be present in a statistically homogeneous record, are generally inapplicable to the tidal front measurements, sometimes because of severe inhomogeneity in the time series (an extreme example is the density record of Fig. 5c), sometimes because of operational constraints limiting the length of useable records. We nonetheless attempt such analysis on selected records, mainly for comparison with the large literature on spectra and cross-spectra of variables observed in the atmospheric boundary layer (ABL). [ABL spectra $S(f)$ are frequently plotted as $\log(fS(f))$ vs $\log(f)$. While not strictly variance-preserving (which would require a linear ordinate), such a presentation does indicate the location of spectral maxima faithfully; we use it to facilitate comparison with ABL results.] First, however, the spectral "noise" levels of the w and σ_t measurements are documented in Fig. 6, showing the spectra as functions of normalized frequency $\hat{f} = f/f_{Ny}$, where the Nyquist frequency is $f_{Ny} = 0.25$ cps. Associated length scales shown at the top are calculated using a constant ship speed of 1 m s^{-1}, appropriate for both of the runs used for w and σ_t noise characterization. These (nonsimultaneous) noise records are simply those with the lowest signal levels encountered during the cruise: the σ_t record is that of Fig. 5d, while noise levels of w are measured in a protected coastal inlet at slack water. Density "noise" is seen to reside predominantly at low frequency (wavenumber). A likely source is small tow depth variation within a vertically stratified water column, but residual lateral water mass variation, left as turbulence decays in a decreasing tidal flow, is another possibility. In contrast, noise in w is concentrated at high frequency (wavenumber). This difference in the spectral distribution of noise variance tends to make noise level records uncorrelated, and hence lower the effective noise level in the calculated flux.

We wished to use the longest available run (run 1, that of Figs. 3 and 5a) to form signal spectra. Since we know that the frontal turbulence zones are geographically fixed (on the timescale of the ship passage), and since ship speed over the ground V_g varied considerably over this run, it was necessary to reexamine the usual conversion from frequency f to horizontal wavenumber k via $k = f/\bar{V}_g$ using record mean $\bar{V}_g$. Before calculating a transform, we have attempted to convert the measured

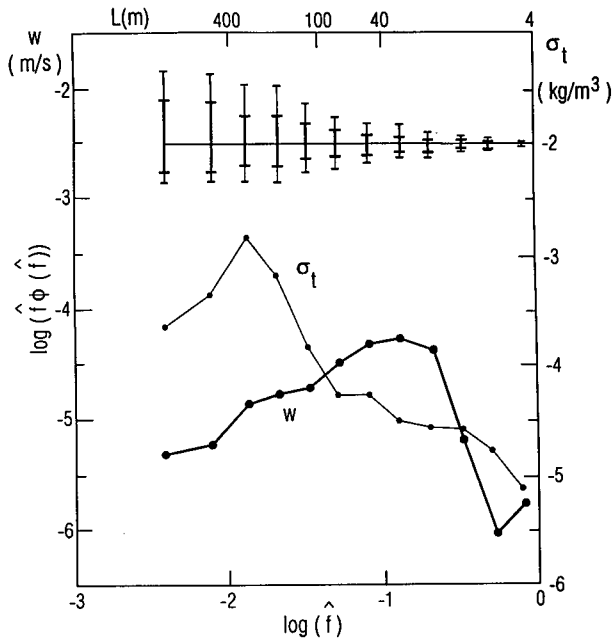

FIG. 6. "Noise" spectra of σ_t and w. These (nonsimultaneous) "noise" records are simply those with the lowest signal levels encountered during the cruise: the σ_t record is that of Fig. 5d, whereas noise level of w is measured in a protected coastal inlet at slack water. The 95% confidence limits shown at the top are largest for σ_t. Noise in w is concentrated at high frequency (wavenumber), while density "noise," arising through small variations in tow depth and/or residual water mass variations, is predominantly at low frequency (wavenumber). This difference in the spectral distribution of noise variance tends to make noise level records uncorrelated, hence the lower effective noise level in calculated flux.

time series to a spatial series, by computing spatial sampling locations with the time series $V_g(t)$ of ship speed, then interpolating to uniform spatial sampling $dx = \bar{V}_g dt$. This procedure is not strictly legitimate, as it involves multiple interpolations between successive measured points when $V_g > \bar{V}_g$, but it is the best possible under the circumstances. [In fact, the resulting wavenumber spectra differ only slightly from straightforward frequency spectra (not shown), probably as a result of the broadband nature of the spectra of variables in high Reynolds number turbulence. We thus feel that it is acceptable to use time (frequency)-based calculations elsewhere, as in the cospectral calculations to follow.] The interpolated "spatial" series were processed as half-overlapped blocks of length M: individual blocks were cosine-windowed before transforming, and the resulting spectra were first block-averaged, then band-averaged over constant logarithmic bandwidth. Figure 7a shows the resulting autospectra for σ_t, w, and the instantaneous flux. The σ_t spectrum is computed from the raw σ_t time series, since it contains information at frequencies higher than those associated with (smoothed) w: however before forming the flux

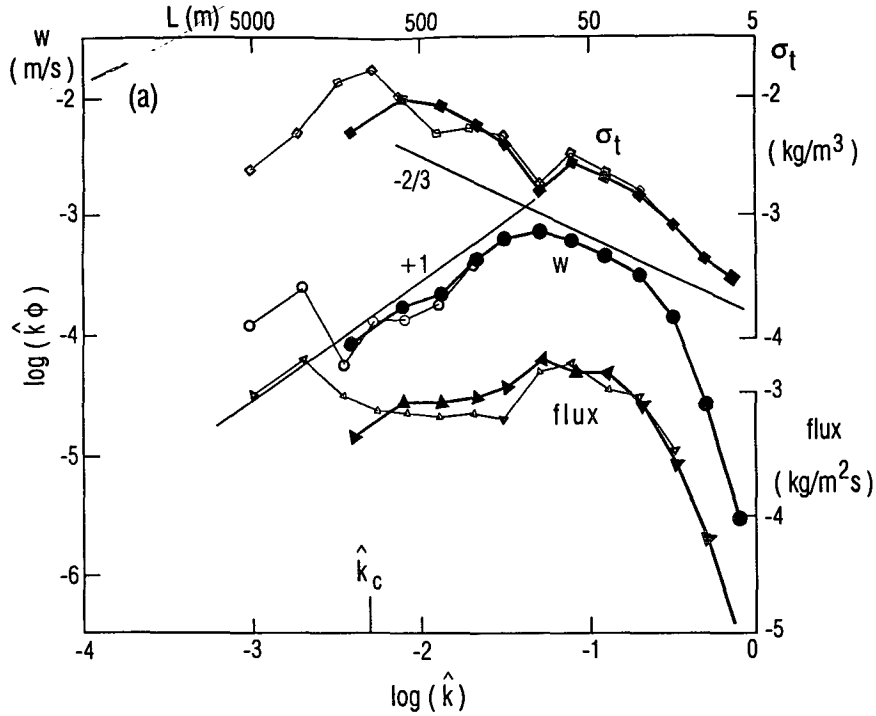

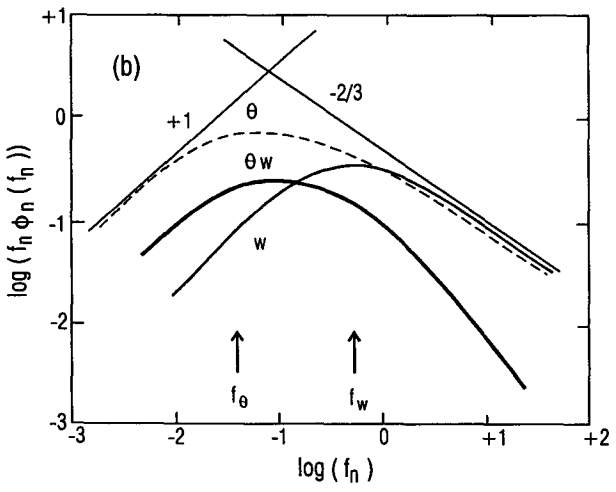

FIG. 7. (a) Power spectral densities of σ_t (squares), w (circles), and the product $\sigma_t w$, labeled flux, for run 1 (see Fig. 5a). Solid (open) symbols are spectral estimates using block size M = 512(2048). Because of substantial variation in ship speed over the ground (V_g), the original time series were converted to spatial series before transforming (for details see text). The resulting spectra are presented as functions of $\hat{k} = k/k_{Ny}$, horizontal wavenumber k normalized by Nyquist wavenumber $k_{Ny} = f_{Ny}/\bar{V}_g$, f_{Ny} = 0.25 cps, and $\bar{V}_g$ = 1.25 m s^{-1}. $\hat{k}_c$ marks the 3 dB point of a (phase preserving) high-pass filter subsequently applied to the density time series. (b) Schematic of the results of measurements in the atmospheric boundary layer (Kaimal et al. 1972), showing plots of spectra of temperature θ, vertical velocity w, and flux θw, as functions of normalized frequency $f_n = nz/U$, where n is frequency and U is mean wind speed. The spectra exhibit various consistent features, namely: (i) a spectral peak of θ at lower frequency (f_θ) than that (f_w) of w, (ii) falloff of all spectra as k^{+1} at low wavenumber, (iii) approach of both θ and w spectra to expected inertial subrange behavior ($k^{-2/3}$) at high wavenumber, and (iv) location of the flux spectral peak between those of θ and w. Many of these same features are seen in the tidal front spectra of (a).

time series, σ_t is low-pass filtered (preserving phase) as w. Theoretical error bars (not plotted) for the heavy curves (M = 512) are equal to the inner error bars in Fig. 6: differences between values obtained with two different block sizes give another view of the likely statistical error.

From years of observation, various spectral characteristics of ABL turbulence have become familiar. As seen in the schematic of Fig. 7b (redrawn from Fig. 17 of Kaimal et al. 1972), plots of (normalized) spectra of fluctuation temperature θ, vertical velocity w, and flux θw exhibit the following features in this representation:

(i) a spectral peak of θ at lower frequency (f_θ) than that (f_w) of w

(ii) falloff of all spectra as k^{+1} at low wavenumber

(iii) at high wavenumber, approach of both θ and w spectra to expected inertial subrange behavior ($k^{-2/3}$) and

(iv) location of the flux spectral peak between those of θ and w.

Most of these same features are seen in the tidal front spectra of Fig. 7a. The main difference is that the present flux spectrum appears to extend to higher wavenumbers, that is, at least into the inertial subrange of the w spectrum, than the atmospheric flux spectrum as shown in Fig. 7b. Such behavior is however consistent with marine ABL temperature flux spectra measured by Pond et al. (1971).

The flux spectrum shown in Fig. 7a reveals the size of structures that may contribute to the density flux: for the crucial phase relationship between density and vertical velocity, it is necessary to examine the cospectrum. Inhomogeneity of the measured flows and the need to achieve acceptable confidence intervals on the cospectrum necessitated ensemble averaging, that is, averaging over a number of nonconsecutive realizations. The cospectrum shown in Fig. 8 is an average of cospectra from nine segments, chosen from portions of runs over which the towed flux estimate was positive and fulfilled a "strict" criterion for significance (details in the following section). For ensemble averaging, the individual cospectra were normalized by the autospectral densities of the two time series: ensemble-averaged values were further band averaged over the same logarithmic bands used for the spectra in Fig. 7a. If the normalized averaged cospectrum is represented by Co + iQu, Fig. 8a shows the real part Co (heavy line), as well as the coherence coh $\equiv (\mathrm{Co}^2 + \mathrm{Qu}^2)^{1/2}$ (light line) used in estimating error bounds for phase $\equiv \arctan(-\mathrm{Qu}/\mathrm{Co})$ (Jenkins and Watts 1968). The maximum values of coherence, ~0.5, are comparable to those observed in high Reynolds number ABL turbulence (Pond et al. 1971). Although Co exhibits apparent countergradient flux at the lowest wavenumbers, these wavenumbers contribute relatively little to the total flux variance, which is dominated by downgradient contributions over a decade of nondimensional frequency from $\log(\hat{f}) = -2$ to -1 (Fig. 7a). Because of the low-pass filtering used on w and σ_t, the flux will, if anything, be underestimated by the observational resolution. Comparison with the ABL results mentioned previously suggests that this effect may be relatively small; that is, the actual flux cospectrum may roll off at frequencies not much higher than those we have been able to resolve. Phase (Fig. 8b) is stable near zero over the range of frequencies that dominate the flux. Despite the amount of averaging, error bounds are still large at low wavenumbers due to limited degrees of freedom and at high wavenumbers because the coherence is low, error bars are plotted only where they are less than ±50°.

The above comparisons suggest that the fields we measured were associated with high Reynolds number turbulence. Where buoyancy flux was significantly nonzero, the flux was carried by scales that convert to

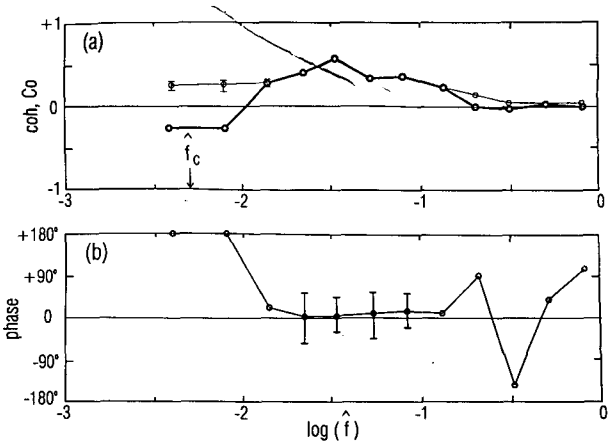

FIG. 8. Because of large inhomogeneity in coastal flows, reliable cospectra can only be achieved by ensemble averaging: this figure shows the result of averaging over portions of flux records that produced positive (downgradient) flux estimates (see section 3e). (a) Coherence (light line, coh = $(\mathrm{Co}^2 + \mathrm{Qu}^2)^{1/2}$, where Co and Qu are, respectively, the normalized co- and quadspectra) reaches a maximum of about 0.5. The normalized cospectrum Co (heavy line), which integrates to the flux, indicates possible countergradient flux (restratification) at the lowest wavenumbers: however, this contributes little to the overall flux, as seen in the plots of Fig. 7a. The associated phase spectrum (b) indicates that over nearly a decade of frequency, including a major portion of the measured flux, phase is near 0°, and significantly different from the value of ±90°, which would be associated with internal wave motion.

nondimensional frequencies greater than 0.01. Thus, we chose $\hat{f}_c = 0.005$ (shown in Fig. 8a) as the cutoff of a high-pass Butterworth filter, which was applied (forward and backward to conserve phase) to the σ_t time series before proceeding to form flux estimates: ρ designates this filtered time series, which will be used as "fluctuation density" in the towed flux calculation. For "fluctuation vertical velocity," we use the w time series without high-pass filtering. As explained below, this retention of low frequencies in the w signal allows identification and rejection of segments with nonzero average w due to ship "trapping" in the main frontal convergence zone.

e. The towed flux calculation

Time series of instantaneous flux, calculated by multiplying ρ and w time series such as those seen in Fig. 5, contain both down- and upgradient values: determining reliable density flux values requires averaging over a number of estimates. The 95% confidence interval of an estimate F made by averaging over dof *independent* estimates f_i is given by s_F:

$$s_F = \pm 1.96\sigma_f/(\mathrm{dof})^{1/2}, \qquad (4)$$

where $\sigma_f^2 = [\sum_{i=1}^{\mathrm{dof}} (f_i - F)^2]/(\mathrm{dof} - 1)$. However, consecutive flux estimates are not necessarily independent if the variance-containing features are oversampled, as is the case with our measurements. Thus, the

first question that arises is how to determine dof, the number of independent flux estimates within a number of estimates averaged.

It seems reasonable that dof should in some way count the number of features of the size that dominates the flux. Considering Fig. 7a and remembering that the observed flux spectrum may be artificially cut off at high wavenumber by the low-pass filtering employed, it appears that the flux is carried by scales comparable to those of w, *as resolved by our measurements.* Thus, we chose to identify the characteristic flux scales with those of measured w, typically of order of 40–100 m. An averaging length of $P = 200$ (pings), corresponding to a length of 400 m at the normal ship speed, spans only 4–10 cycles of the dominant vertical velocity features. This is not a particularly large number of degrees of freedom (dof) to use in (4) above, and one might wish to increase it. For a time series with constant statistics (i.e., constant σ_f), we may decrease s_F by increasing the length of record over which the flux is averaged, hence increasing dof. Unfortunately, inspection of typical flux records shows substantial inhomogeneity over the record lengths, associated with the method of measuring physically fixed structures (fronts) by ship traverses. This inhomogeneity means that an attempt to increase statistical reliability by increasing the averaging length eventually fails, because as the record length P (hence dof) increases, so does σ_f. Thus the final choice of P, the number of measured flux values to average, becomes a trade-off between the need for flux estimates to be statistically reliable (P large), yet local (P small).

Lenschow et al. (1994) have recently determined the systematic and random errors associated with estimating turbulent fluxes from finite amounts of data. The systematic (bias) error [Lenschow et al., Eq. (30)] is a decreasing function of TI/τ_f, where TI is the time interval of the measurement and τ_f is the integral timescale of the flux correlation function. Assuming an exponential correlation function, τ_f can be estimated as $\tau_f = \omega_m^{-1}$ where ω_m is the (radian) frequency of the peak of $\omega\Phi(\omega)$, the flux spectrum multiplied by frequency. Taking $\hat{f} = \hat{k} = 5 \times 10^{-2}$ as an estimate of the frequency of this peak (see Fig. 7a), and converting to dimensional radian frequency yields $\tau_f \sim 13$ s. For averaging length TI = 400 s (200 pings), the expressions of Lenschow et al. then predict that the flux will be systematically *under*estimated by ~6%. The random error [Lenschow et al., Eq. (48)] is a function of both TI/τ_f and r_f, the correlation coefficient between ρ' and w'. With TI = 400 s and a value of $r_f = 0.25$ (the mean of r_f over those towed flux estimates that satisfy significance tests to be defined shortly), the random error component of a single estimate is nearly 100%: ensemble averaging over the combined results of all available runs is clearly necessary to decrease the random component of error to acceptable levels. The challenge is to identify appropriate ensembles for averaging, given the likelihood that positive density flux within the strong frontal turbulence is followed by negative flux (partial restratification) downstream. We have used a two-stage process, first calculating averaged flux values together with ad hoc uncertainty limits that reveal unreliable estimates associated with low dof, then classifying these estimates by comparison with similar calculations made using randomized phase [a suggestion apparently first made by B. Ruddick, and used subsequently by Yamazaki and Osborn (1993) and Fleury and Lueck (1994)]. The resulting classes form the basis for subsequent investigation of turbulent efficiency (section 5).

In the first stage, flux estimates and error bounds are calculated as follows. We first choose a maximum value for P (typically 200 or 400 pings) on the basis of the perceived scales of inhomogeneity in the flux time series. Both ρ and w time series are then segmented into blocks of length P, starting with the first point $j = 1$ of each series. For each resulting block (n), block means $\bar{\rho}$ and $\bar{w}$ are calculated, and the associated flux estimate $F_{n1} = [\Sigma(\rho' w')]/P$ is formed, with $\rho' = \rho - \bar{\rho}$ and $w' = w - \bar{w}$.

Because P does not contain a very large number of flux-carrying structures, a segment starting from another point $(n-1)P + 1 < j \leq nP$ may have a substantially different segment mean, so that the associated estimate F_{nj} differs from F_{n1}. The flux calculation is thus carried out for all possible different starting points $(n-1)P + 1 < j \leq nP$ and averaged, giving estimates of block mean F_n and standard deviation σ_n:

$$F_n = [\Sigma F_{nj}]/P$$

$$\sigma_n = ([\Sigma(F_{nj} - F_n)^2]/(P-1))^{1/2}.$$

Since calculation of F_n uses points from $(n-1)P + 1$ to $(n+1)P - 1$, the value F_n is assigned to nP, and consecutive estimates can be thought of as half-overlapped.

It is then necessary to estimate dof, the number of degrees of freedom (i.e., truly independent values) within the data that enters F_n. As discussed above, we determine a lower bound dof from the w time series, under the assumption that the dominant flux scales are not (much) larger than the dominant measured vertical velocity scales. Since the average value F_n actually uses data over a length $L = 2P$, from $(n-1)P + 1$ to $(n+1)P - 1$, an algorithm determines c = number of cycles = (number of zero crossings)/2 in the length L of the vertical velocity w, then assigns $c_n = c/2$. In practice, to count a zero crossing, the algorithm requires that it be followed by a run of at least r points of the same sign: the choice $r = 3$, corresponding to horizontal wavelengths of $O(12\text{ m})$, combines with the shape of the vertical velocity spectrum at high wavenumber to minimize the effects of small-scale noise on the determination of c_n. Finally, we assume that dof $= c_n$ and that a 95% error bound on F_n is $s_{Fn} = \pm 1.96\sigma_n/c_n^{1/2}$.

The presence of velocity or density structure at scales comparable to the averaging length increases s_{Fn} in one or both of two ways. First, the block averages $\bar{w}$ and $\bar{\rho}$ in (5) will vary over the length L, with possible increase in the variance σ_n of the set F_{nj}, hence in s_{Fn}. A second effect is a decrease in c_n (in fact, $c_n = 0$ can occur) as measured by the number of zero crossings of w, again increasing s_{Fn}. This method of using w to estimate dof provides a means of automatically flagging those sections of the record where the ship was trapped in a frontal downwelling.

Finally, the effects of small variations in the relative position of the Doppler and the CTD are assessed by repeating the above flux calculation twice, with the ρ time series shifted relative to the w time series by ± 1 ping (remembering that horizontal displacement of the CTD by more than ± 2 m, equivalent to ± 1 ping would have resulted in resetting the tow position).

For each averaging interval, the procedure outlined above supplies a local mean value of density flux $F = \langle \rho' w' \rangle$, along with an uncertainty s_F, which includes the effects of a limited number of degrees of freedom (the n subscripts are henceforth dropped for simplicity). In addition, two shifted flux estimates, F^R and F^L, assess the degree to which small variations in CTD tow position may have affected the measurement. Defining $F\text{set} = [F, F^+, F^-, F^R, F^L]$, where $F^+ = F + S_F$, $F^- = F - S_F$, the upper and lower uncertainty limits on F are determined as $\max\{F\text{set}\}$, $\min\{F\text{set}\}$, respectively.

To accept a computed towed flux value as significantly different from zero, a minimum requirement is that all values in Fset be of the same sign. In the second stage of estimating statistical significance, more stringent criteria are devised, using results from a companion "randomized phase" calculation. Every "real" estimate F is an average (over the number P of different starting indices) of P individual lengths of w data multiplied by simultaneous ρ data. If instead we choose the starting index for the ρ subset *randomly* from among the P possible values and carry out the same calculations outlined above for F and s_F, the resulting "random" flux R is expected to average to zero, within error bounds $\pm s_R$, defining the set $R\text{set} = [R, R^+, R^-]$, $R^+ = R + s_R$, $R^- = R - s_R$. Using this set as well, we define levels of confidence for the measured flux (assumed positive: changes for negative flux are obvious) as

1) stringent: $\min\{F\text{set}\} > \max\{R\text{set}\}$—that is, the real set nowhere overlaps the random set

2) relaxed: $R < \min\{F\text{set}\} < \max\{R\text{set}\}$—that is, the minimum value of the real set is allowed to fall below $R + s_R$ but not below R

3) minimal: $F\text{set} > 0$.

Note that these levels are defined as noninclusive; for example, set 2 does not include set 1.

Figure 9 shows the fluxes, random fluxes, and associated error bounds described above, as calculated for the three records of Fig. 5. The symbols used for the flux estimates represent their classification, as described above. Most of the estimates from run 1 (Fig. 9a) fulfill one of the two higher criteria, as do the countergradient estimates near the end of run 2 (Fig. 9b). High variance combines with low dof to make flux estimates unreliable in the first part of run 2, while almost all run 3 estimates are insignificant (Fig. 9c).

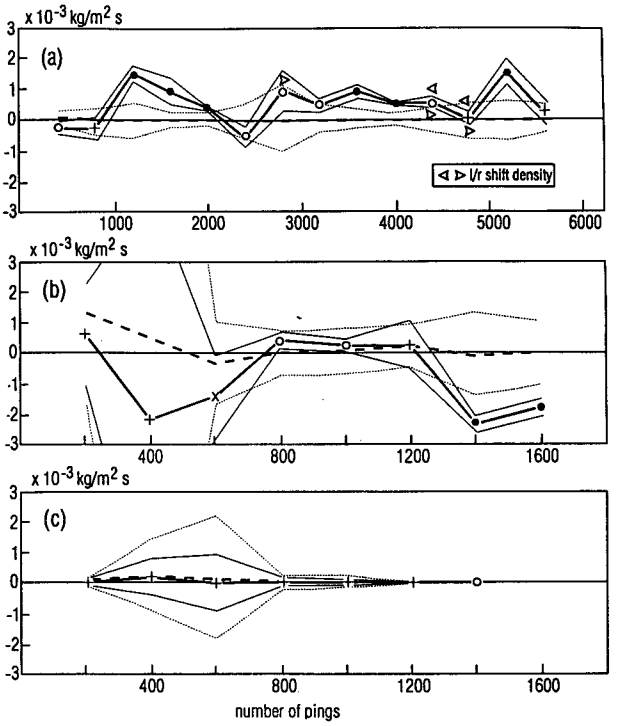

FIG. 9. For the records (a) run 1, (b) run 2, and (c) run 3 shown in Fig. 5, solid lines join calculated values of buoyancy flux (heavy) and error bounds (light); left- and right-shifted fluxes are visible as triangles where sufficiently different from the centered value. Dashed lines denote "random" fluxes (heavy) and their error bounds (light), as used to classify the level of confidence of the actual flux estimate. Different symbols are used to denote flux estimates that fulfill stringent (solid circles), relaxed (open circles), or minimal (×) criteria or are not significantly different from zero (+): for details see text.

4. The calculation of dropped fluxes

The dropped flux estimates F_ϵ and F_χ, as defined in Eqs. (1) and (2), require estimates of ϵ, χ, T_z, and ρ_z from Chameleon profiles. These estimates then need to be combined in such a way that they can be compared to the towed flux estimates discussed in section 3. While the towed flux estimates were derived from continuous records (400–800 pings long at fixed depth), the dropped estimates are discrete vertical snapshots, with 10–20 profiles per towed flux estimate. How should the profiler data be combined to determine fluxes for comparison to towed flux estimates, and what are the relative uncertainties in dropped flux estimates?

a. Computation of ϵ, χ

The computation of ϵ from shear probe measurements on Chameleon is discussed in detail by Moum et al. (1995). Briefly, the spectra of velocity gradient fluctuations computed from two shear probes mounted on Chameleon are integrated and the isotropic form for the dissipation tensor assumed, so that only 2 (of 12) terms are used in the estimate of ϵ. Full resolution of the dissipation spectrum requires integration to the Kolmogoroff wavenumber, $k_s = (\epsilon/\nu^3)^{1/4}$ [rad m^{-1}]. Because the shear probes have finite spatial resolution (−3 db at about 70 cpm) the highest wavenumbers of the dissipation spectra are not resolved when ϵ is sufficiently high. This is a particular problem for the tidal flow measurements, as the turbulence is so energetic (Fig. 3). At the highest values observed ($\epsilon \approx 10^{-4}$ m^2 s^{-3}), only about 30% of the variance is resolved by integrating to 70 cpm [according to the empirical and supposedly universal form of the spectrum of Nasmyth (1970)]. A correction in the wavenumber (practically, frequency) domain for spatial attenuation of the shear probes (Ninnis 1984) increases the resolved variance to 40% at 10^{-4} m^2 s^{-3}.

In practice, however, we integrate to 0.5 k_s, or 45 cpm, whichever is smaller (after the spatial correction is applied). An iterative scheme is employed to determine the lost variance due to incomplete spectral integration. The universal spectral coefficients are scaled to dimensional units using Kolmogoroff scaling and ϵ' determined by integrating the measured spectrum over the range 2–45 cpm. Another estimate, ϵ_{unv}, is then obtained by integrating the scaled universal spectrum over the same bandwidth. If the two estimates agree within 5%, we accept the result. If not, the estimate ϵ' is corrected by a factor ϵ'/ϵ_{unv}. New integration limits are then determined and a new estimate ϵ_{unv} obtained. This is repeated until the two estimates agree to within 5%. The final estimate of ϵ is that obtained by integrating the properly scaled universal spectrum to k_s. An unknown level of uncertainty in this procedure is due to the assumption of universality of the Nasmyth form for the dissipation scale shear spectrum and is larger for larger corrections.

Another problem that is accentuated in this particular flow regime is the determination of flow speed past the sensors (U_s), used in computing both ϵ and χ. In the estimate for ϵ, flow speed appears as U_s^4, introducing a large source of error if incorrect. In most open ocean experiments, the rate of descent of the vehicle through the water column is assumed to be equivalent to the flow speed past the sensors; that is, $U_s = dz/dt$. This is incorrect when the vehicle does not respond exactly and/or instantaneously to significant vertical velocities in the water column, or when the vehicle is tilted and follows its nose through the water (i.e., has a horizontal component to its path). In the tidal flows, vertical velocities can be many tens of cm s^{-1} (Fig. 3) and vehicle tilts were occasionally up to 7°. For a measurement of flow speed independent of descent rate, we used a two-axis Marsh–McBirney electromagnetic velocity sensor deployed on Chameleon's nose. Comparison of flow speed determined in this way to descent rate indicated differences up to 0.2 m s^{-1}. For all of the ϵ and χ calculations made here, U_s was determined from the electromagnetic velocity sensor.

The temperature variance dissipation rate χ was calculated under the assumption of dissipation-scale isotropy by scaling the temperature gradient spectrum obtained from the differentiated signal of an FP07 temperature sensor in the inertial–convective subrange (assuming the Batchelor form for the spectrum; Dillon and Caldwell 1981). The form of the correction for incomplete integration of the spectrum appears in the appendix of Peters et al. (1988). Again, an unknown level of uncertainty is introduced in the corrections applied for incomplete spectral integration, due to the assumption of universality of the Batchelor form for the temperature spectrum.

b. Flux computations

In assessing the uncertainties in the microscale parameters ϵ and χ which enter F_ϵ and F_χ, our basic premise is that the scales of the turbulence are large and horizontal homogeneity exists over the length of record used to compute each towed flux estimate. Over horizontal record lengths of 400–800 m, we may expect vertical homogeneity over at least a few meters. To test this expectation, we computed ϵ and χ over 1-m intervals for all profiles within the interval of a single towed flux estimate and used these as the basic dataset to determine the appropriate vertical averaging interval for flux computations.

Individual 1-m estimates of ϵ from all of the profiles in each towed flux estimate and over vertical intervals of ±3, 5, 10 m from the tow depth were treated as independent samples. Smaller intervals were not considered because the number of data points was too small. Larger intervals were not considered because of the likelihood of including the effects of surface- and ship-influenced mixing, which is distinct from mixing at the tow depth. We considered these samples to be representative of ϵ within a homogeneous turbulence field occupying a pseudovolume determined by the depth interval and the horizontal averaging length used for the towed flux estimates. The arithmetic mean value of ϵ was computed, following the suggestion of Davis (1994) that this is more accurate than other possibilities in cases where the true distribution function is not well known and the sample size is small. Uncertainty was assessed as the 95% bootstrapped limits (Efron and Gong 1983) on the mean, reflecting the natural variability of ϵ within the sample volume. The relative uncertainty was defined as (upper 95% limit−lower 95% limit)/mean. Since 1) only requires estimation of ϵ (to

within 0.05%, which is the uncertainty in $\rho_0 g^{-1}$), this also effectively represents the relative uncertainty in F_ϵ. We define Eset = $[F_\epsilon, F_\epsilon^+, F_\epsilon^-]$, where F_ϵ^+ is the upper 95% uncertainty limit and F_ϵ^- the lower 95% limit.

A comparison of the different depth interval estimators shows the relative uncertainty at 10 m to be generally smallest (Fig. 10). However, infrequent but large deviations (>2) occurred in the 10-m estimate but not the others, suggesting that effects uncharacteristic of the tow depth were included. Consequently, we chose ±5 m as the interval for computing fluxes. Scatterplots (Fig. 11) indicate that, for the most part, the result is not much different if we choose 3, 5, or 10 m.

The analysis of the uncertainty in the F_χ estimate is slightly different, because as well as estimation of an average value of χ, it requires determination of local gradients of T and ρ. It is not practical to calculate these gradients on the 1-m scale of the χ estimates. Instead, the gradients were determined by first reordering individual profiles of T and ρ into stable configurations (Thorpe 1977), then computing gradients over the entire depth interval ($d \pm 5$ m) chosen for analysis. Then F_χ was calculated for each profile, using the average of all 1 m χ values in the profile and the profile mean gradient values. Hence, although each estimate of F_χ is made over a greater depth range than that (1 m) used for individual F_ϵ estimates, fewer F_χ estimates are available for computing the uncertainty over the ensemble of profiles within the averaged towed flux intervals. As a result, uncertainty limits, again determined by the bootstrap method, are relatively larger for F_χ than for F_ϵ. We define Cset = $[F_\chi, F_\chi^+, F_\chi^-]$, where F_χ^+ is the upper 95% uncertainty limit and F_χ^- the lower 95% limit.

An example of the three flux estimates computed from the combined datasets is shown in Fig. 12 for run 1. Figure 12a shows the individual dropped estimates of F_ϵ and F_χ calculated as described above from Eq. (1) (using an arbitrary value of $\Gamma_o = 0.2$) and Eq. (2), respectively. The averaged flux estimates, with uncertainty limits, are seen in Fig. 12b. The dropped fluxes represent averages over all profiler estimates within the record length used to calculate the towed flux estimate. Two features common to the complete dataset are seen in this plot. First, F_χ is typically less than F_ϵ. Second, while the dropped fluxes are by definition positive, the towed flux estimate is sometimes negative.

5. Mixing efficiencies

Comparison of towed and dropped estimates of density flux is most readily accomplished in terms of the flux coefficients Γ_o and Γ_d, as defined by Eqs. (1) and (3). Here Γ_o and Γ_d are functions of the flux estimates F, F_ϵ, and F_χ, and their uncertainties can be defined from general uncertainty analysis (Coleman and Steele 1989) as functions of the uncertainties in the independent variables, determined as described in the previous two sections. Expressing the uncertainty in Γ_o as $\delta\Gamma_o$ (and similarly for Γ_d),

$$\delta\Gamma_o = \Gamma_o\left(\frac{\delta F}{F} + \frac{\delta F_\epsilon}{F_\epsilon}\right)$$

and

$$\delta\Gamma_d = \Gamma_d\left(\frac{\delta F_\epsilon}{F_\epsilon} + \frac{\delta F_\chi}{F_\chi}\right),$$

where δF, δF_ϵ, and δF_χ are the uncertainties computed for individual flux estimates, as detailed above. These forms are used for the uncertainty limits in the analysis plots to follow.

Because individual flux estimates contain relatively few degrees of freedom, we use the ensemble results of all data taken during the cruise in order to ask the questions: 1) Is the towed flux estimate related to the microscale estimates? 2) If so, what are the proportionality constants? That is, does $\Gamma_o = \Gamma_d$ as expected?

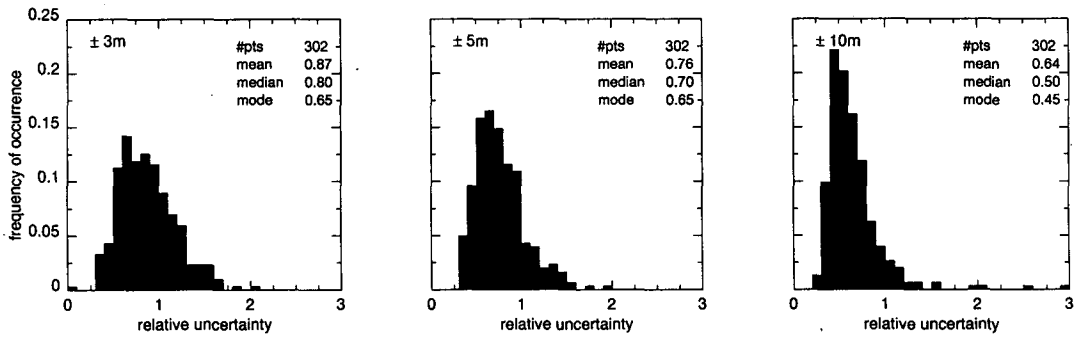

FIG. 10. Histograms of the relative uncertainty in estimates of ϵ averaged over all of the profiles obtained within a single towed flux estimate (usually 200–400 pings, and 5–10 profiles). Relative uncertainty is defined as the difference between upper and lower 95% bootstrap limits divided by the mean of the sample population consisting of 1-m vertical averages of ϵ (i.e., the sample size is 70 for 7 profiles averaged ±5 m from tow depth). Results obtained by averaging ±3, 5, 10 m from tow depth are shown.

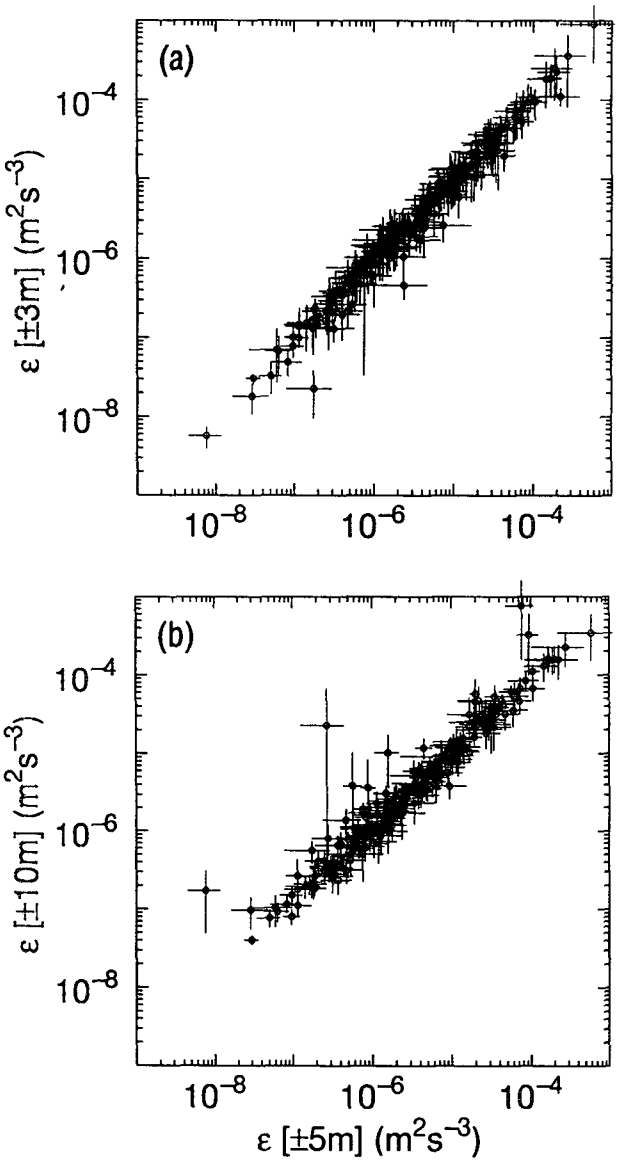

FIG. 11. (a) Direct comparison of ϵ averaged over ±5 m (abscissa) and ±3 m (ordinate) from tow depth. (b) Direct comparison of ϵ averaged over ±5 m (abscissa) and ±10 m (ordinate) from tow depth. Ninety-five percent bootstrap limits are shown for each estimate as a representation of the uncertainty due to natural variability of the turbulence within the pseudovolume of the average.

The first question is addressed in Fig. 13, which presents logarithmic scatterplots of the microscale flux estimates vs the absolute value of the towed flux: triangles denote "normal" downgradient density flux, circles denote countergradient (restratifying) flux. Because the relaxed class (bottom, Fig. 13c and 13d) has both a larger number of members and larger error bounds than the stringent class (top, Fig. 13a and 13b), it is difficult to see individual points in plots with error bars: thus, duplicate panels, with and without error bars, are presented. Both classes show positive correlation between each of the microscale estimates and the magnitude of the towed flux, regardless of its sign.

The answer to the second question is contained in Fig. 14, where values of the two flux coefficients Γ_o and Γ_d are shown (again with and without error bars) for the stringent (upper plots) and relaxed (lower plots) classes. For reference, a horizontal dashed line is placed at the value (0.2) commonly used in Eq. (1) to derive flux from measured ϵ. It is immediately obvious that values of Γ_o are larger than those of Γ_d. This result is essentially the same for both classes, with larger scatter within the relaxed class. Comparison of error bars in Figs. 14a and 14b shows that the error bounds associated with Γ_d are considerably larger than those of Γ_o. Since the estimates of ϵ are common to both estimates of Γ, the larger errors are associated with the determination of F_χ, as noted in section 4b. Finally, there is a suggestion that the mean value of Γ_o is larger for negative than for positive values of the towed flux.

The relationships between Γ_o and Γ_d and between values of Γ_o with difference in sign of the towed flux are further examined in Fig. 15, which displays histograms of the logarithms of Γ_o (upper panels) and Γ_d (lower panels). Stringent and relaxed classes are combined for this analysis, since there is no obvious difference between the two in Figs. 13 and 14, apart from the size of the error bars. Existing theory (Gurvich and Yaglom 1967) suggests that dissipation-scale quantities such as ϵ and χ (and hence their ratio, as used in Γ_d) should be lognormally distributed in high-Reynolds number turbulence, which is homogeneous and isotropic. However, the turbulent flows of our measurements span a range of Reynolds numbers, are clearly inhomogeneous on the frontal scale at least, and have an unknown degree of isotropy. In addition, our measurements of ϵ and χ are made from a one-dimensional transect, hence may be better described as a cut-off-lognormal distribution, as derived by Davis (1995). Thus, the present use of the logarithm is less a response to theoretical considerations than a result of observing (Fig. 14) that estimates of both Γ_o and Γ_d vary by at least a factor of 1000, hence must be transformed in some way to allow statistical significance to be attached to "mean" values.

The left-hand plots of each set contain values calculated from segment-mean values, $\Gamma_d = F_\chi/F_\epsilon$ and $\Gamma_o = F/F_\epsilon$ for subsets stratified by the sign of F. The subsets associated with positive and negative F contain 91 and 33 values, respectively (Table 1), relatively small numbers which produce the rather ragged appearance of these histograms. However, we have estimated uncertainty limits for the measured fluxes and only expect the "true" values to lie within the sets {Fset}, {Eset}, and {Cset}, partly due to natural (statistical) variability and partly through uncertainty of measurement technique (the right- and left-shifted flux values). There is no real reason to expect that the "true" value

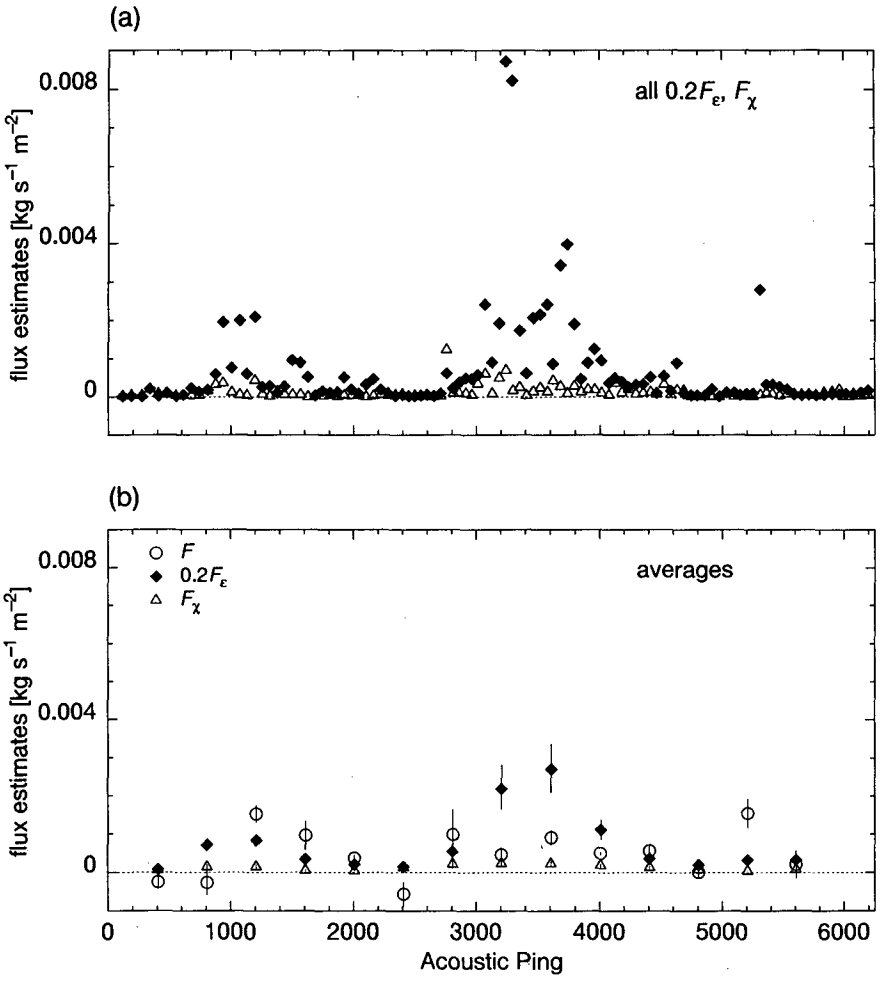

FIG. 12. (a) Values of the dissipation-based density fluxes $\Gamma_o F_\epsilon$ (solid diamonds; using a standard value of $\Gamma_o = 0.2$) and F_χ (open triangles, as in 12b), as determined from individual Chameleon profiles during run 1. (b) Averaged values of F_ϵ and F_χ are computed over the number of profiles within the record length used to compute the towed flux F. This comparison of the three flux estimates that can be made from our data reveals two typical characteristics; while the dissipation-based fluxes are necessarily positive, F is sometimes negative, and $F_\chi < 0.2F_\epsilon$.

of Γ is the result of forming the ratio of mean values, rather than, say, the ratio of the mean value of the numerator, divided by the mean plus uncertainty of the denominator. Distributions generated by computing values over the much larger sets of all possible permutations of $\{F\text{set}\}$ and $\{E\text{set}\}$ for Γ_o or of $\{C\text{set}\}$ and $\{E\text{set}\}$ for Γ_d are shown as the right-hand panels of Fig. 15 and will henceforth be referred to as the augmented sets. Table 1 lists mode, median, and geometric mean associated with the histograms of Fig. 15; the superscript a refers to the augmented dataset. Ensemble mean values shown at the bottom of Table 1 for Γ_o and Γ_d were computed from the mean value of $\log\Gamma$ (or geometric mean value of Γ). Ninety-five percent confidence limits on the geometric mean value of Γ were estimated in two different ways. First, under the assumption that the sample distributions of the logarithms of Γ_o, Γ_d, Γ_o^a, and Γ_d^a are approximately lognormal, 95% confidence limits on the geometric mean were determined as $10^{(\mu \pm 1.96\sigma n^{-1/2})}$, where μ is the sample mean value of $\log\Gamma$, σ is the sample standard deviation, and n is the number of samples. Another estimate, which requires no assumption concerning the form of the sample distribution, is the bootstrap method (Efron and Gong 1983), and 95% bootstrapped confidence intervals on the geometric mean were computed. Each range is listed at the bottom of Table 1 and illustrated in Fig. 16.

With reference to Fig. 16, we draw the following conclusions:

1) $\Gamma_d < \Gamma_o$. Regardless of the sign of F, the geometric mean values from all four sample distributions of Γ_d are significantly less than those from all four sam-

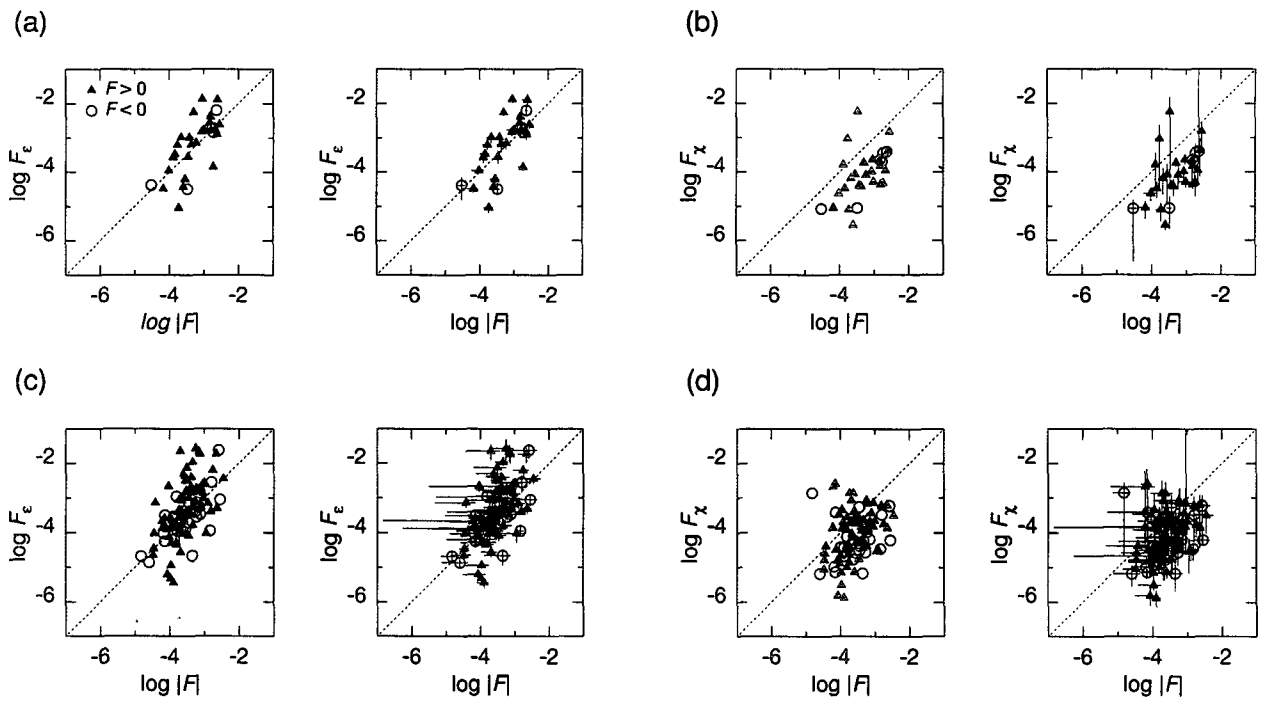

FIG. 13. (a) and (b) Scatterplots of F_ϵ and F_χ vs $|F|$ for towed flux data satisfying the stringent criterion (see text, section 3e): open circles and filled triangles distinguish between negative and positive F. The right-hand panels of each pair include uncertainty limits. (c) and (d) Same variables, for data satisfying the relaxed criterion.

ple distributions of Γ_o. Both methods of estimating 95% confidence limits confirm this. Also, there is no distinction between the geometric mean values of Γ_d for positive and negative values of F.

2) $\Gamma_o(F > 0) < |\Gamma_o|(F < 0)$. This is significant at the 95% confidence level for the augmented datasets, although there is some overlap for the original datasets.

In the following discussion of these results of the direct and indirect determinations of Γ, we will use the values obtained from the augmented sets, since the characteristics of the original sets appear very similar.

6. Discussion

A mean value of $\Gamma_o \approx 0.7$ (Table 1) implies a mean value of $R_f \approx 0.4$. This is approximately twice the value of about 0.2 that normally emerges from oceanic observations (which of course are actually made using Γ_d), from (low Reynolds number) laboratory flows (Linden 1979; Rohr et al. 1984; Rohr and Van Atta 1987), from dimensional arguments (Ivey and Imberger 1991), and from (again low Reynolds number) direct numerical simulations (Itsweire et al. 1993). It is also twice the value determined from our own estimate of Γ_d using coincident data. Can we reconcile the greater implied mixing efficiency of this particular flow field, the dependence of Γ_o on the sign of F, and finally, the discrepancy between Γ_o and Γ_d?

a. Do tidal flows mix more efficiently?

There are a number of reasons why it *does* seem possible that the turbulent fields of our measurements could operate to mix density more efficiently than previously reported flows. First, is the fact that tidal front turbulence has a typical Reynolds number $\mathrm{Re} \sim 10^7$ (taking typical rms turbulent velocity $w \sim 0.2$ m s^{-1}, length scale $\ell \sim 50$ m, and $\nu \sim 10^{-6}$ m^2 s^{-1}), much larger than those typical of laboratory flows or instabilities in the stratified interior of the open ocean, and very much larger than those achievable by present numerical simulations. Available "theory" for the dependence of R_f on dimensionless parameters such as Re and Froude number Fr is based on scaling relationships, validated against laboratory flows or numerical simulations in which $\langle \rho' w' \rangle$ can be directly determined (Gargett 1988; Ivey and Imberger 1991; Itsweire et al. 1992). Thus far, attention has been focused mostly on Fr dependence because such test flows are characterized by low Reynolds numbers, of order 10^2 or smaller. There are no validated predictions as to the magnitude of R_f expected when $\mathrm{Re} \sim 10^7$, and that the value of R_f obtained here does not agree with previous values may merely result from the very large difference in Re. This does not suggest a mechanism but merely acknowledges that none of the experiments, theories, or simulations to date have examined such high Re flows; hence their results may not apply here.

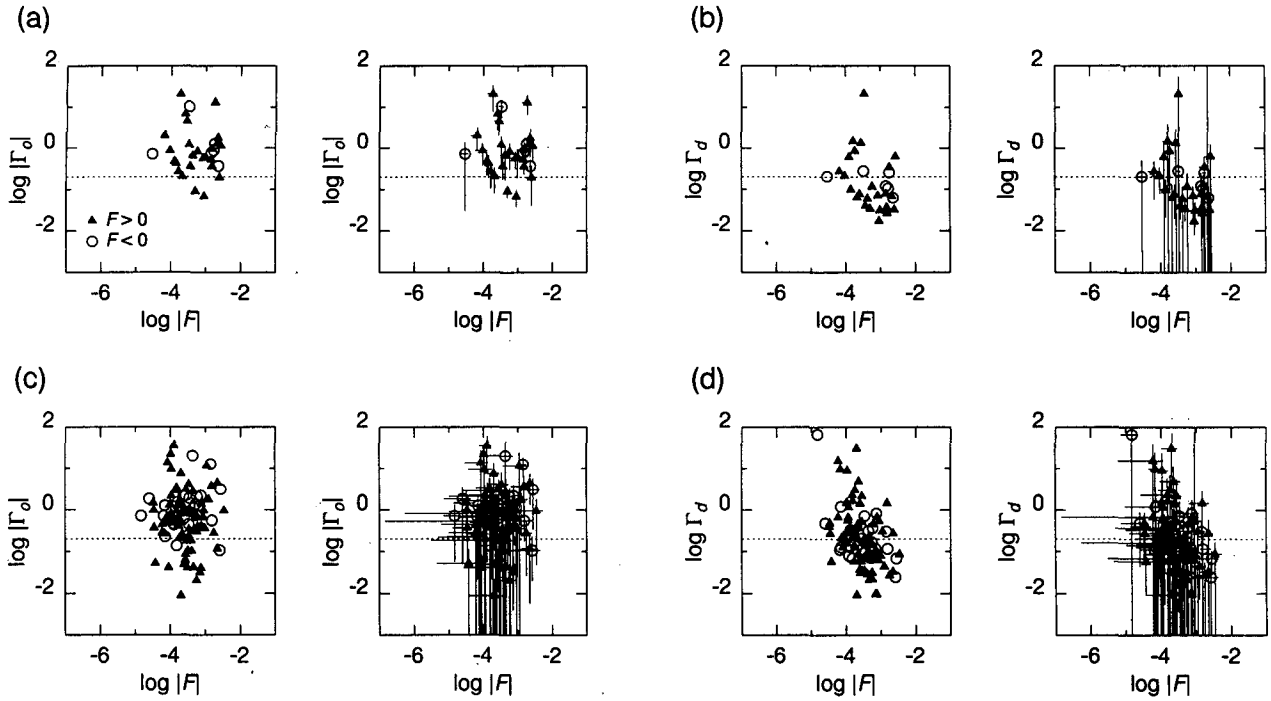

FIG. 14. (a) and (b) Scatterplots of mixing efficiencies Γ_o and Γ_d vs $|F|$ for towed flux data satisfying the stringent criterion (see text, section 3e): open circles and filled triangles distinguish between negative and positive F. The right-hand panels of each pair include uncertainty limits. (c) and (d) Same variables, for data satisfying the relaxed criterion.

A more mechanistic argument for a larger efficiency may lie in the physical process by which tidal front turbulence is generated. First consider the original argument justifying $R_f \ll 1$. For turbulence resulting from instability of the vertical shear of a mean horizontal flow, Stewart (1959) considered equations for the separate components of turbulent kinetic energy. He showed that TKE was initially supplied to $\langle u'^2 \rangle$, the component in the direction of the mean shear, then redistributed via pressure forces into the other two components, including the vertical. Loss to buoyancy affects only the vertical component $\langle w'^2 \rangle$, while viscous losses occur in all three components. Thus, since R_f is the ratio of the loss of energy to buoyancy to the total loss of energy to buoyancy and viscosity, we should expect $R_f \ll 1$ (provided, as is known to be the case, the redistribution by pressure forces is inefficient relative to the dissipative decay mechanism). It is hard to argue with this analysis, given the underlying assumptions. Consider, however, the difference that arises if it is assumed that the source of TKE is not the instability of a vertically sheared horizontal current, but instability of a large-scale vertical flow sustained by mean horizontal convergence, supplying energy directly to the vertical component $\langle w'^2 \rangle$ of TKE. Then the amount of energy available for working against buoyancy is not constrained by the inefficient transfer from a horizontal component, and the above argument that $R_f \ll 1$ is consequently weakened. In this case, we may conclude only that $R_f < 1$. In a separate investigation (Gargett and Foreman 1994, personal communication), mean flow velocities from a tidal model are being used to predict frontal positions in a manner analogous to that of Simpson and Hunter (1974), who used a turbulent timescale based on the vertical shear of horizontal velocity, $\tau \propto (\partial U/\partial z \sim U/H)^{-1}$, where U = barotropic tidal velocity, H = depth of fluid. It appears that a timescale $\tau_w \propto (\partial W/\partial z)^{-1}$ inversely proportional to the vertical shear of vertical velocity, supported by horizontal convergence $(\partial U/\partial x + \partial V/\partial y)$ of the mean horizontal velocities, provides a more accurate predictor of frontal positions, lending credence to the above argument that the tidal fronts are flows in which one may not necessarily expect $R_f \ll 1$.

b. *Dependence of* Γ_o *on the sign of* F

A difference between the values of Γ_o with the sign of the towed flux estimate, statistically significant in the augmented dataset, may also be physically reasonable. Consider the equation for TKE, written schematically as

$$-s = \epsilon + b, \tag{5}$$

where $b = g\rho_0^{-1}\langle \rho' w' \rangle = g\rho_0^{-1} F$ is the buoyancy flux. The definition $R_f \equiv -b/s$ arises from a simplified version of (5) in which the source of TKE is shear production; that is, it is assumed that $s = \langle u'w' \rangle U_z < 0$.

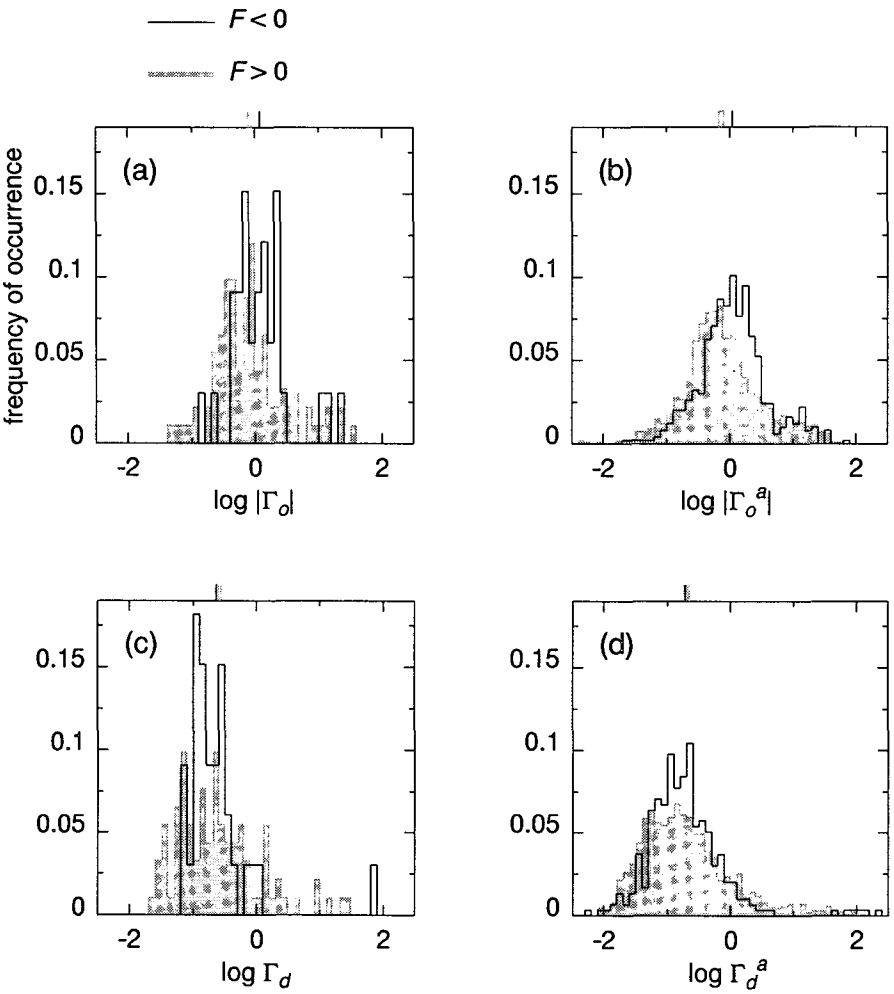

FIG. 15. (a) Histograms of Γ_o using the data shown in Figs. 14a and 14c: the distribution associated with downgradient flux $F > 0$ is shaded and that with countergradient flux $F < 0$ is outlined. (b) Histograms of the augmented set of Γ_o values, generated by forming all possible permutations over {*F*set}/{*E*set} (see text, section 3e). The resulting sample population is 15 times greater than the original in Fig. 15a. (c) and (d) Same as (a) and (b) except for the dissipation-based efficiency Γ_d; here the augmented set is formed by all possible permutations of {*C*set}/{*E*set}, and the resulting population is nine times larger than the original.

The definition $\Gamma_o \equiv b/\epsilon$ requires no distinction of production mechanism, so for now we simply consider s to represent the sum of all terms, other than buoyancy flux and dissipation, which normally appear in the TKE equation [e.g., local time rate of change, advection of TKE by the mean flow, diffusion of TKE, local redistribution of TKE by pressure forces: see Osborn (1980), Ivey and Imberger (1991), Gargett (1993)]. The dissipation rate $\epsilon > 0$ always represents a sink of TKE. Generally, in stratified turbulence it is assumed that $b > 0$ also represents a TKE sink. However, local restratification may occur, in which case $b < 0$. In convectively driven turbulence, the primary source of TKE is b (Shay and Gregg 1986), also requiring $b < 0$. When we consider s as only a shear production term, we infer $s < 0$ (Tennekes and Lumley 1972). If instead s is an advective or diffusive flux of TKE, or a local time rate of change of TKE, s may have either sign. We consider the limiting cases [noting that s and b cannot both be >0, according to Eq. (5)]:

(*i*) $s < 0, b > 0$.

This includes the case of shear production of TKE ($s < 0$) acting to increase the potential energy of a stably stratified fluid by moving dense fluid upward ($b > 0$). It could also include the case of decaying turbulence, where the local time rate of decay provides an energy source $s < 0$. Here,

$$\Gamma_o > 0.$$

(*ii*) $s \leq 0, b < 0$

TABLE 1. Statistics of Γ_o and Γ_d corresponding to the histograms in Fig. 15. The superscripts a refer to the augmented datasets described in the text. Ninety-five percent confidence intervals for the geometric mean were computed both by the bootstrap method (upper set of parentheses beneath the geometric mean) and using normal statistics (lower set of parentheses). Figure 16 summarizes the corresponding ranges in geometric means.

	Γ_o		Γ_o^a		Γ_d		Γ_d^a	
	$F > 0$	$F < 0$	$F > 0$	$F < 0$	$F > 0$	$F < 0$	$F > 0$	$F < 0$
Number of points	91	33	1365	495	91	33	819	297
Median	0.63	−1.0	0.63	−1.0	0.20	0.13	0.13	0.16
Mode	0.89	−0.71, −2.2	0.71	−1.1	0.07, 0.22	0.16	0.14	0.22
Geometric mean	0.81	−1.2	0.73	−1.1	0.25	0.23	0.20	0.19
	(0.63, 1.0)	(−0.90, −1.6)	(0.69, 0.78)	(−1.0, −1.2)	(0.20, 0.33)	(0.17, 0.34)	(0.18, 0.22)	(0.16, 0.22)
	(0.61, 1.1)	(−0.85, −1.7)	(0.67, 0.79)	(−1.0, −1.2)	(0.18, 0.35)	(0.16, 0.34)	(0.18, 0.23)	(0.16, 0.22)

This is the case of combined shear and buoyancy production of TKE. Equation (5) requires $|\epsilon| > |b|$. Hence,

$$-1 \leq \Gamma_o < 0,$$

where $\Gamma_o = -1$ is attained in cases of steady-state convection.

(iii) $s > 0$, $b < 0$

In this case, s is a sink of TKE, requiring $b < 0$ and $|b| > |\epsilon|$; hence

$$\Gamma_o < -1.$$

Our observation of $\Gamma_o \approx 0.7$ where measured $F > 0$ corresponds to case *(i)*. It appears that during the increasing phase of the ebb, a shear term of some sort must act as a source, supplying not only the dissipation and buoyancy flux sinks, but also the effective sink associated with local time increase of TKE. As the ebb decreases, decay of TKE may for some time provide a source sufficient to supply both continuing downgradient density flux as well as dissipation. Note that while previously reported values of $\Gamma_d > 0$ have been assumed to correspond to case *(i)*, they may equally well correspond to cases *(ii)* or *(iii)* since our observations indicate that the same value of Γ_d is obtained *regardless of the sign of b*. Our observation of $\Gamma_o \approx -1.1$ where measured $F < 0$ may correspond to either case *(ii)* or case *(iii)*.

c. *Why is* $\Gamma_d < \Gamma_o$?

Since estimates of Γ_d have been the basis of observational determinations of oceanic density flux (or equivalently density diffusivity $K_\rho = -\langle \rho' w' \rangle \rho_z^{-1}$), it is important to discover the source of this discrepancy, and we will examine various ways in which the observational methods may have affected values of Γ_d. First, however, we reexamine derivation of Eq. (3) for Γ_d, and compare it to other versions used in the literature.

1) DERIVATION AND INTERPRETATION OF Γ_d

There are two different ways of deriving Eq. (3), both involving two fundamental assumptions. The first is that the equation of state of seawater is a linear function of T and S, so density $\rho = \rho_0(1 - \alpha T + \beta S)$, vertical gradient of density $\rho_z = \rho_0(-\alpha T_z + \beta S_z)$, where T_z and S_z are the mean vertical gradients of T and S, and fluctuation density $\rho' = \rho_0(-\alpha T' + \beta S')$. The second is that the fluctuations T' and S' are gen-

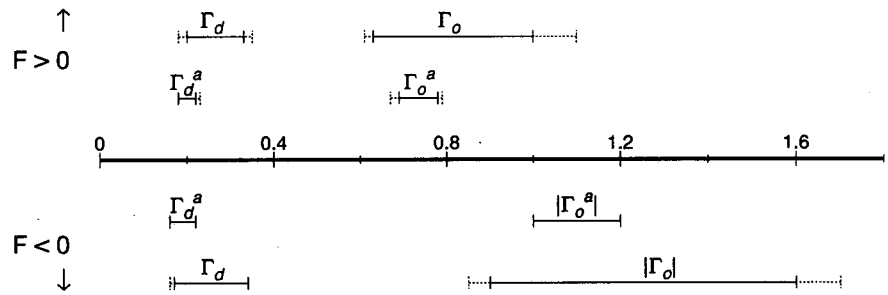

FIG. 16. Ranges of 95% confidence of the geometric mean values of the distributions shown in Fig. 15 estimated using the bootstrap method (solid lines) and assuming normal statistics (dashed lines). Based on this analysis, we can state, with 95% confidence, that the geometric mean values of Γ_d and Γ_d^a are the same, independent of the sign of F, but they are significantly different from Γ_o. Also, the geometric mean value of Γ_o^a when the flux is positive is less than that of $|\Gamma_o^a|$ when the flux is negative.

erated by overturning in the mean T and S gradients, and related by $T'/S' = T_z/S_z$ on the scales which dominate the fluctuation variances and turbulent fluxes. This is certainly a reasonable assumption for the variance-containing scales, though less certain for the flux-containing scales, which may be somewhat smaller. Given these assumptions

$$\langle \rho' w' \rangle = \rho_0(-\alpha\langle w'T' \rangle + \beta\langle w'S' \rangle)$$
$$= \rho_0(1 - R_\rho^{-1})(-\alpha\langle w'T' \rangle), \quad (6)$$

where $R_\rho \equiv \alpha T_z/\beta S_z$ is the stability ratio. The steady-state temperature variance balance proposed by Osborn and Cox (1972),

$$\langle w'T' \rangle T_z = -\langle \chi \rangle/2,$$

allows the temperature flux in Eq. (6) to be written in terms of dissipation rate χ and mean gradient T_z. Equating the resulting expression for density flux to that provided by the steady-state TKE equation proposed by Osborn (1980), that is, Eq. (1), and noting that $N^2 = g\alpha T_z(1 - R_\rho^{-1})$ yields the expression we have used for Γ_d:

$$\Gamma_d = (1 - R_\rho^{-1})\frac{g\alpha\langle \chi \rangle}{2\langle \epsilon \rangle T_z} = \frac{\langle \chi \rangle N^2}{2\langle \epsilon \rangle T_z^2}. \quad (7)$$

While the original expression for the dissipation flux coefficient (Oakey 1982) was derived assuming that density was determined only by T and would be incorrect where this was not the case, most subsequent work (Oakey 1988; Peters et al. 1988; Moum et al. 1989) has used the above form. It can be demonstrated that, under the assumptions given above, this form is consistent with interpretation of Γ as the ratio of $\langle \chi_{pe} \rangle$, the rate of dissipation of available potential energy η, to $\langle \epsilon \rangle$, the rate of dissipation of TKE. The usual definition of available potential energy

$$\eta \equiv \frac{1}{2}\left\langle \left(\frac{\rho'}{\rho_0}\right)^2 \right\rangle \left(\frac{g}{N}\right)^2 \quad (8)$$

(Dillon 1984; Gregg 1987) shows that a conservation equation for η is obtained from that of averaged fluctuation density variance. Such an equation is often written down directly; here, we remember that what is actually conserved is not density, but T and S individually. In simplified form, the fluctuation T and S variance equations are

$$\frac{1}{2}\frac{\partial}{\partial t}\langle (T')^2 \rangle = -\langle T'w' \rangle T_z$$
$$- D_T\langle (\nabla T')^2 \rangle + \text{other terms}, \quad (9)$$

$$\frac{1}{2}\frac{\partial}{\partial t}\langle (S')^2 \rangle = -\langle S'w' \rangle S_z$$
$$- D_S\langle (\nabla S')^2 \rangle + \text{other terms}, \quad (10)$$

where the other terms are those discarded in the usual simplified variance balance originally suggested by Osborn and Cox (1972). Normalized fluctuation density variance is given by

$$\left\langle \left(\frac{\rho'}{\rho_0}\right)^2 \right\rangle = \langle (-\alpha T' + \beta S')^2 \rangle = \alpha^2\langle (T')^2 \rangle$$
$$- 2\alpha\beta\langle T'S' \rangle + \beta^2\langle (S')^2 \rangle. \quad (11)$$

Since it has been assumed above that $T'/S' = T_z/S_z$ at scales dominating fluxes and variances, it is only consistent here to take $\alpha\beta\langle T'S' \rangle = \beta^2 R_\rho \langle S'^2 \rangle$; hence,

$$\left\langle \left(\frac{\rho'}{\rho_0}\right)^2 \right\rangle = \alpha^2\langle (T')^2 \rangle + \beta^2(1 - 2R_\rho)\langle (S')^2 \rangle. \quad (12)$$

Multiplying Eq. (9) by α^2, Eq. (10) by $\beta^2(1 - 2R_\rho)$, and adding yields the equation for normalized fluctuation density variance

$$\frac{1}{2}\frac{\partial}{\partial t}\left\langle \left(\frac{\rho'}{\rho_0}\right)^2 \right\rangle = -\left\langle \frac{\rho'w'}{\rho_0} \right\rangle \frac{\rho_z}{\rho_0}$$
$$- \left[\alpha^2 \frac{\langle \chi \rangle}{2} + \beta^2(1 - 2R_\rho)\frac{\langle \chi_S \rangle}{2} \right], \quad (13)$$

where $\chi_S = 2D_S\langle (\nabla S')^2 \rangle$ is the dissipation rate of salinity variance. Multiplying through by $(g/N)^2$ and using the argument of Gregg (1987) that universality of spectral shapes at energy-containing scales implies $\chi_S/\chi = (S_z/T_z)^2$, this can be rewritten as

$$\frac{\partial \eta}{\partial t} = \frac{1}{2}\left(\frac{g}{N}\right)^2 \frac{\partial}{\partial t}\left\langle \left(\frac{\rho'}{\rho_0}\right)^2 \right\rangle$$
$$= -\left\langle \frac{\rho'w'}{\rho_0} \right\rangle \frac{\rho_z}{\rho_0}\left(\frac{g}{N}\right)^2 - \langle \chi_\eta \rangle, \quad (14)$$

where

$$\langle \chi_\eta \rangle = (1 - R_\rho^{-1})^2\left(\frac{g\alpha}{N}\right)^2 \frac{\langle \chi \rangle}{2} \quad (15)$$

is the dissipation rate of available potential energy. Hence, substituting for N^2 in terms of T_z and R_ρ,

$$\frac{\langle \chi_\eta \rangle}{\langle \epsilon \rangle} = (1 - R_\rho^{-1})^2\left(\frac{g\alpha}{N}\right)^2 \frac{\langle \chi \rangle}{2\langle \epsilon \rangle}$$
$$= (1 - R_\rho^{-1})\frac{g\alpha\langle \chi \rangle}{2\langle \epsilon \rangle T_z} = \Gamma_d. \quad (16)$$

A similar but slightly different form for Γ_d is that proposed by Gregg (1987):

$$\Gamma_d^G = (1 + R_\rho^{-2})\left(\frac{g\alpha}{N}\right)^2 \frac{\langle \chi \rangle}{\langle \epsilon \rangle}. \quad (17)$$

This differs from Γ_d by a factor of 2 and the factor of $(1 + R_\rho^{-2})$ in place of $(1 - R_\rho^{-1})^2$. The factor of 2

appears to result from defining the rate of dissipation of η as $\langle\chi_{pe}\rangle/2$ [Gregg 1987, Eq. (58)], then using only $\langle\chi_{pe}\rangle$ in the expression for Γ. With this correction, the abnormally large value of $\Gamma_d^G = 0.58$ reported by Seim and Gregg (1994) reduces to 0.29, still slightly larger but more comparable to the bulk of dissipation-based values reported in the literature. Making an additional modification for the different factor of R_ρ would further reduce this value, to ~0.23.

The factor of $(1 + R_\rho^{-2})$ *would* appear in place of $(1 - R_\rho^{-1})^2$ in Eq. (16) *if* it were assumed that $\langle T'S'\rangle = 0$ in Eq. (f): thus, the appropriate form of Γ_d depends upon the degree of correlation between T' and S' at flux-carrying scales. For our measurements, correlation coefficients for T' and S' exceed 0.97 even when T' and S' are formed by high-pass filtering with cutoff frequency $f = 0.1\, f_{Ny}$, that is, retaining only scales considerably smaller than those containing the scalar variance (cf. Fig. 7a). For typical magnitudes of R_ρ, the difference between the factor $(1 - R_\rho^{-1})^2$ associated with perfect correlation and that $(1 + R_\rho^{-2})$ associated with zero correlation is rather slight in subarctic gyres ($R_\rho \ll 0$), but can be substantial in subtropical gyres ($R_\rho > 1$). Thus it is important to estimate the $T'S'$ correlation at flux-containing scales for a broad variety of turbulent flows, although we expect that in general it will be found to be closer to 1 than to 0.

We have thus ascertained that Eq. (3) is the form used in (most) other determinations of Γ_d, and is consistent with interpretation of Γ_d as the ratio of the rate of dissipation of available potential energy to that of turbulent kinetic energy. The fact that the range of our Γ_d measurements (0.16–0.23, 95% confidence limits of Γ_d^a; Table 1) lies within the range of most previous determinations indicates that our estimates are not systematically biased low relative to other available datasets. Finally, then, we must consider whether there are any features of the way in which we and others compute the parameters involved in Eq. (7), which might bias the resulting values of Γ_d relative to Γ_o.

2) Possible sources of bias in observational determination of Γ_d

We first look for possible sources of bias in the observational determination of the dissipation quantities involved in Eq. (7). As pointed out in section 4a, both ϵ and χ values are corrected for loss of variance at unresolved high wavenumbers by fitting to universal spectra. However, since ϵ enters both Γ_o and Γ_d, it cannot be responsible for a bias of Γ_d *relative* to Γ_o: thus, we focus on possible bias in the determination of χ. Because we are working in high Reynolds number turbulence, temperature gradient variance almost always extends to scales smaller than those the thermistor resolves. Thus, χ is routinely determined by correcting the observed variance by a factor based on the variance of a "universal" form of the scalar spectrum, derived for the one-dimensional spectrum by Gibson and Schwarz (1963) from Batchelor's (1959) original three-dimensional formulation. Unfortunately, the degree of universality of the passive scalar spectrum is considerably more controversial than that of the turbulent velocity spectra. Using measurements that resolved both velocity and temperature spectra through dissipation ranges, Gargett (1985) demonstrated a significant degree of variation, dependent upon Re, in the low wavenumber "inertial" and "inertial–convective" ranges, coupled with consistent associated changes in the dissipation range. Miller (1991) observed comparable effects at the low wavenumber ranges resolved by his measurements of conductivity fluctuations in a turbulent jet, while Sherman and Davis (1995) report that temperature observations from a cycling profiler cannot be described by a universal form. The dissipation range is characterized in Batchelor's theory by a parameter q, which determines the high-wavenumber roll-off: the higher the value of q, the lower the wavenumber of the roll-off, all other factors being equal. The observations of Gargett (1985) showed that q was dependent upon Re, ranging from $q \approx 12$ for the highest Re, most isotropic flows, through $q \approx 4$ for lower Re flows, which had developed demonstrable anisotropy down to dissipation scales in velocity. The present values of χ were calculated with a correction factor based on $q = 4$, while the high Re characteristics of the tidal channel flows suggest that $q = 12$ might have been more appropriate. However, since a high-q gradient spectrum rolls off at a lower wavenumber than a low-q spectrum (see Gargett 1985, Fig. 8b), correcting for lost variance with the assumption that $q = 4$ will produce an *overestimate* of χ if q is actually larger. Such an error would thus cause our estimate of Γ_d to be, if anything, an overestimate, increasing the difference between Γ_o and Γ_d. We conclude that nonuniversality of this sort could not be responsible for persistent underestimation of Γ_d.

Equation (7) for Γ_d also requires estimates of R_ρ and T_z [Γ_d is actually computed using values of N^2 and T_z^2, i.e., the second formula of Eq. (7), but this is equivalent to using a locally determined value of R_ρ in the first expression]. We find it hard to imagine a process that could result in the factor $(1 - R_\rho^{-1})$ being systematically low both in the region of our measurements, where R_ρ is small and negative, and in the subtropical waters where most other measurements of Γ_d have been made and where R_ρ is much larger and positive. The final possible source of systematic bias is T_z, ideally the mean temperature gradient in which overturning initially occurs, as a source of systematic bias. As pointed out in Thorpe's initial paper (Thorpe 1977), reordering observed temperature will only recreate the initial gradient if no diffusion has occurred in the time interval between the initial overturn and the observation. Since this time interval and the integral effect of diffusion over it are unknown in any particular

case, the depth-local gradient determined by reordering observed values can only be considered a lower bound to the original gradient. Thus, an observational estimate of Γ_d by Eq. (7) will be again, if anything, an *overestimate* due to such inaccuracy in determining the initial value of T_z.

3) CONSEQUENCES FOR THE INTERPRETATION OF F_ϵ

In summary, we have not been able to identify a source of persistent observational underestimation of Γ_d, moreover one which would be common to all extant measurements, in both the high Re tidal fronts of the present dataset and the relatively low Re instabilities in the stratified interior of the deep ocean. Of course large values of Γ_o relative to Γ_d would also result if the towed flux values were systematically overestimated. While this possibility cannot be definitely discounted, we think it is unlikely. First, measurement sources of error in determination of flux by the direct correlation technique (such as variation in CTD position relative to the Doppler beam) will generally act to reduce any correlation by introducing random error into the phase of w relative to ρ. Second, recall that systematic error in the flux should also be in the direction of underestimation (Lenschow et al. 1994). We *have* used conditional sampling (selecting those record segments in which the flux signal was significant relative to the accompanying randomized phase "noise") to ensure that our distributions contain only flux estimates of a quantifiable level of significance. By thus excluding towed flux values that are not significantly different from "noise," it is possible that we have biased our result high by preferentially excluding small values. To test the effect of including all values for statistical analysis, the values in Table 1 and Figs. 15 and 16 were recomputed as prescribed, but without conditional sampling. The effect was to reduce the geometric mean values of $\Gamma_o^a(F > 0)$ from 0.73 to 0.55 and $|\Gamma_o^a|(F < 0)$ from 1.1 to 0.97, while 95% confidence ranges are still exclusive. This effect is thus not sufficient to produce agreement between our values of Γ_o and Γ_d.

A final problem with direct flux measurements is the vexing question of whether the averaging that has been done is "appropriate" to the process(es) involved, hence gives a meaningful value for efficiency. We cannot claim to have a definitive answer to this question for the tidal fronts we have measured. Certainly, each of our flux estimates is itself an average over many individual values, some positive and some negative: the *average* is then either positive or negative, with a level of significance which we have quantified. The resulting efficiencies are characteristic of high Reynolds number flow regimes with either average positive or average negative turbulent fluxes. However, the larger question is the *net* effect of mixing in the tidal fronts. For that, the present estimates of efficiencies in regions of positive and negative density flux would have to be combined with estimates of the time individual water "parcels" spend in each of these regions during a transit of the front. Net efficiency would then involve the average values of positive and negative fluxes, weighted by residence times, a procedure which will in general yield a net mixing efficiency smaller than the value found to characterize the regions of positive flux. One might be tempted to perform a simple-minded average over our available significant datasets: this temptation should be avoided, as there is absolutely no reason to assume that our random sampling of these fronts in the course of ship traverses would produce anything approaching the right distribution of water particle "residence times." Our subjective impressions of residence times (obtained mainly by observing surface and subsurface flotsam moving along and finally out of the front) are that particles that become caught up in the chaotic flows at the front spend many tens of minutes within these regions, characterized by positive density flux: on finally exiting the front, they reenter nearly unperturbed mean tidal flow, thus passing rapidly through those regions characterized by negative fluxes. If this impression is correct, net efficiency would close to that measured in the regions of positive flux: we proceed with discussion of the results on this basis.

Our results suggest that the "dissipation technique" for determining the efficiency of turbulent mixing has two major problems: The first is a fundamental inability to determine even the *sign* of the flux; clearly, Γ_d is a positive definite quantity whereas the real turbulent flow has regions of both positive and negative average density flux. This situation is not surprising, as the mere presence of dissipation says nothing about the source of the variance being dissipated. The source might be shear instability, but may equally well be time decay of the turbulent fields, motion associated with restratification, or destabilizing surface buoyancy flux. While not surprising, the result *is* disconcerting since oceanic measurements of Γ_d have been interpreted as associated with strictly positive average density flux. Since the present results show no difference in the mean values of Γ_d associated with positive and negative averaged density flux, it is equally possible that oceanic dissipation is associated with strictly negative density flux. While such an extreme possibility may seem unlikely, it cannot be discounted without independent information on the sign of the flux: indeed, Holloway (1988) presents a self-consistent scenario in which dissipation is associated with countergradient density flux on all scales less than or equal to the overturning scale.

The second problem is that even when the average density flux *is* positive, $\Gamma_d < \Gamma_o$. Use of Γ_d in place of Γ_o in Eq. (1) will underestimate the associated flux by a factor of ~ 3. How might this discrepancy arise? There are many assumptions that enter either or both derivations of Eq. (7) for Γ_d. Two major assumptions seem satisfied. First the equation of state of seawater is reasonably linear over a restricted range in T and S, a

high correlation between T' and S' well into the flux-containing range was demonstrated, and we have checked that $(T')^2/(S')^2 = T_z^2/S_z^2$ to within 10%, using towed data from the CTD as well as profile data from Chameleon. Second, given the high Re characteristics of the flows (section 3d), it appears justified to use isotropic relations for estimating ϵ and χ from measurements of only one gradient component. What remains?

There is the possibility that determination of χ_η from measured T variance and assumptions of the universal nature of scalar spectra fails in situations, such as ours, where salinity is the major stratifying property. Also, the balances assumed for turbulent kinetic energy and available potential energy (or equivalently scalar variance) in the models of Osborn (1980) and Osborn and Cox (1972), respectively, may be too simplistic. These balances discard many of the terms present in the full balance equations, using in particular assumptions that the flows are steady-state and spatially homogeneous (for a summary, see Gargett 1993). Without reconsidering all of the discarded terms, consider as an example retention of the time-derivative term in the equation for available potential energy, written schematically as

$$\frac{d\eta}{dt} \equiv t_P = b - \langle \chi_\eta \rangle, \tag{18}$$

where the total time derivative (following the motion) is the sum of the time rate of change at a fixed point and the advective rate of change; that is, $d/dt = \partial/\partial t + U_i \partial/\partial x_i$. Since

$$\Gamma_d \equiv \frac{\langle \chi_\eta \rangle}{\langle \epsilon \rangle} = \frac{(b - t_P)}{\langle \epsilon \rangle} = \Gamma_o - \frac{t_P}{\langle \epsilon \rangle}, \tag{19}$$

it is clear that regardless of the sign of Γ_o, $\Gamma_d \leqslant |\Gamma_o|$ if the time rate of change of potential energy t_P has the same sign as the buoyancy flux b. Although not the only possible way to explain the systematic tendency of Γ_d to underestimate Γ_o, such a hypothesis is actually not unreasonable for our measurement situation, in which water parcels are advected through a frontal region. As water enters the front, $t_P > 0$ as $\langle (\rho')^2 \rangle$ is generated by overturning ($b > 0$). As a parcel exits the strong turbulent zone at the front and b changes sign, t_P must also become negative, since then both terms on the rhs of (18) are negative.

Whether such a hypothesis is reasonable in other situations, such as the more sporadic turbulence generated by Kelvin–Helmholtz instabilities in the ocean interior, is unclear. There are only three other published estimates of oceanic Γ_o with which to compare our measurements; as may perhaps be expected for this preliminary stage in the attempt to make direct flux measurements, they give somewhat different results. Using data from a submarine transect ($\sim$1.4 km) of a single sheared mixing layer, Yamazaki and Osborn (1993) argue that the flux-containing structures were resolved and determine a value of $\Gamma_o \sim 0.05$ (this is the arithmetic mean value of all of the flux estimates, regardless of sign; the geometric mean value of only the downgradient flux estimates in Table 1 of Yamazaki and Osborn is also 0.05; there are only four countergradient values), considerably smaller than even the usual value of $\sim$0.2 determined by the dissipation technique. In relation to our results however, this measurement would constitute a single realization, a particular case of high shear and low stratification. Since the ensemble of all our realizations of Γ_o certainly contains values as low as 0.05, the result of Yamazaki and Osborn may simply be a result of limited sampling. The other horizontally measured, correlation-based estimate is that of Fleury and Lueck (1994), who used data from an instrumented towed body in three different regimes, a sharp and turbulent thermohaline interface, the upper thermocline, and a temperature inversion layer near the surface mixed layer base. Because vehicle motion contaminated the low wavenumber measurement of w, the flux calculation used only wavenumbers above a low-wavenumber cutoff $k_{\min}$, and their results require some care in interpretation. In cases where $k_{\min}$ was approximately equal to the Ozmidov wavenumber $k_0 \equiv (\epsilon/N^3)^{1/2}$, their results are equivalent to $\Gamma_o \approx \Gamma_d \approx 0.1$. Elsewhere, as $k_{\min}$ progressively exceeds k_0, Γ_d progressively exceeds Γ_o (cf. Fig. 9 of Fleury and Lueck 1994, which is equivalent to a plot of Γ_d/Γ_o vs $k_{\min}/k_0$). These results form a coherent picture if one assumes that the peak of the flux spectrum is around k_0. Measurements that resolve down to wavenumbers $< k_0$ better resolve the flux; hence, one may expect $\Gamma_o \approx \Gamma_d$. The correlation-based flux would be progressively underestimated as $k_{\min}$ increased beyond k_0 so that the cases with $\Gamma_o < \Gamma_d$ are simply associated with underestimation of the correlation-based flux due to the filtering necessary to reject platform motion. Note, however, that it is the spectrum not of flux but of turbulent vertical velocity w' that has been demonstrated to peak around $(0.5-1)k_0$ in stratified turbulent flows (Gargett et al. 1984). From the extensive ABL results, as well as our spectra (Fig. 7a), the flux is carried by somewhat larger scales (smaller wavenumbers), suggesting that even in the best-resolved cases (i.e., where $k_{\min} \approx k_0$), the true flux may be underestimated by the restriction that $k > k_{\min}$. Indeed, Fleury and Lueck themselves point out that, since none of their cospectra exhibit a maximum (i.e., the cospectra were still rising at the lowest resolved wavenumber), this low wavenumber limit on resolution may have obscured a significant fraction of the total flux. In contrast, the dropped flux estimates of Γ_o obtained by Moum (1995) in the main thermocline are restricted to turbulent patches of vertical extent 0.5–5 m and $k_0^{-1} < 2$ m and so should resolve the flux-containing scales: these estimates of Γ_o

are not much different from 0.2, independent of the sign of the flux.

The apparent difference in the Γ_o values from the open ocean and those obtained in the tidal fronts requires either that

- *all* of the open ocean estimates are too low; and/or
- the present flux estimates are too high; and/or
- the physics really are different.

We have examined reasonable sources of bias in our estimates and believe that there are none sufficient to negate our results. Whereas there may be some reason to suspect deficiencies of sampling and/or resolution in existing open ocean measurements of Γ_o, we have also offered a reasonable scenario for the tidal fronts as locations of greater-than-usual mixing efficiency. The possibility that mixing in coastal areas is not only more energetic but also more efficient than that in the stratified interior of the ocean has obvious importance to the on-going debate about the relative importance of boundary versus interior mixing to the global total. Clearly, a much larger body of direct flux measurements, over a wide range of flow situations, will be necessary to resolve this question of efficiency. Given the importance of the answer, we urge continuing effort toward direct, as well as inferred, measurement of fluxes.

7. Conclusions

We have made measurements of turbulent density flux in a geophysical flow, using both a direct correlation technique and indirect dissipation techniques. Because the flux-carrying structures are large and the flow is spatially nonhomogeneous, the necessary measurement technique (ship traverses of a spatially localized turbulent front) results in relatively few degrees of freedom in any single flux estimate. This problem has been addressed in two steps, first estimating significance by comparison with a companion randomized phase calculation, then forming ensembles of significant estimates over the entire dataset.

Comparison between such ensemble averages of mixing efficiency Γ_o, computed with the correlation flux, and Γ_d, computed with fluxes estimated from simplified balances of turbulent kinetic and available potential energies (the so-called dissipation technique), suggests major difficulties with the latter, at least in this application. The first problem, that the dissipation technique could not differentiate the *sign* of the average density flux, means that this technique must be considered suspect unless there is some other method of determining sign. Second, where density flux *was* positive, the dissipation method appears to underestimate the flux, hence any derived eddy diffusivities, by a factor of approximately 3. It was suggested that (in the present case at least) the reason may lie in time-dependence of the available potential energy, which is not encompassed in the formulation of Osborn and Cox (1972).

Based on the augmented datasets, the difference in the magnitude of Γ_o for negative and positive fluxes was statistically significant. Our consideration of the limiting cases of the TKE equation suggests that it is also physically realizable. Perhaps the value and sign of Γ_o will be helpful in determining the sources of turbulence in future experiments.

Acknowledgments. We are grateful to Ed Llewellyn, George Chase, Mark Dinsmore, and Captain and crew of the CSS *Vector* for their help in collecting the data. A.G. would like to thank Steve Pond for helpful discussions regarding cospectra, and we both thank Eric Kunze for making us think harder about net efficiencies. Oregon State participation in this work was supported by ONR Grant N00014-89-J3211.

REFERENCES

Batchelor, G. K., 1959: Small scale variation of convected quantities like temperature in turbulent fluid. *J. Fluid Mech.*, **5**, 113–133.

Chereskin, T. K., and A. J. Harding, 1993: Modeling the performance of an acoustic Doppler current profiler. *J. Atmos. Oceanic Technol.*, **10**, 41–63.

Coleman, H. W., and W. G. Steele, 1989: *Experimentation and Uncertainty Analysis for Engineers.* Wiley, 205 pp.

Crawford, W. R., 1991: Tidal mixing and nutrient flux in the waters of southwest British Columbia. *Tidal Hydrodynamics,* B. B. Parker, Ed., J. Wiley and Sons, Inc., 855–869.

Davis, R. E., 1995: Sampling turbulent dissipation. *J. Phys. Oceanogr.*, in press.

Dillon, T. M., 1984: The energetics of overturning structures: Implications for the theory of fossil turbulence. *J. Phys. Oceanogr.*, **14**, 541–549.

——, and D. R. Caldwell, 1980: The Batchelor spectrum and dissipation in the upper ocean. *J. Geophys. Res.*, **85**, 1910–1916.

Efron, B., and G. Gong, 1983: A leisurely look at the bootstrap, the jackknife and cross-validation. *Amer. Stat.*, **37**, 36–48.

Farmer, D. M., E. A. D'Asaro, M. V. Trevorrow, and G. T. Dairiki, 1994: Three-dimensional structure in a tidal convergence front. *Contin. Shelf Res.*, **15**, 1649–1674.

Fleury, M., and R. G. Lueck, 1994: Direct heat flux estimates using a towed vehicle. *J. Phys. Oceanogr.*, **24**, 801–818.

Gargett, A. E., 1985: Evolution of scalar spectra with the decay of turbulence in a stratified fluid. *J. Fluid Mech.*, **159**, 379–407.

——, 1988: The scaling of turbulence in the presence of stable stratification. *J. Geophys. Res.*, **93**(C5), 5021–5036.

——, 1993: Parameterizing the effects of small-scale mixing in large-scale numerical models. Vol. 3, *Modelling Oceanic Climate Interactions,* J. Willebrand and D. L. T. Anderson, Eds., NATO ASI Series, Vol. I11, Springer-Verlag, 185–204.

——, 1994: Observing turbulence with a modified acoustic Doppler current profiler. *J. Atmos. Oceanic Technol.*, **11**, 1592–1610.

Gibson, C. H., and W. H. Schwarz, 1963: The universal equilibrium spectra of turbulent velocity and scalar fields. *J. Fluid Mech.*, **16**, 365–384.

Gregg, M. C., 1987: Diapycnal mixing in the thermocline: A review. *J. Geophys. Res.*, **92**(C5), 5249–5286.

——, E. A. D'Asaro, T. J. Shay, and N. G. Larsen, 1986: Observations of persistent mixing and near-inertial internal waves. *J. Phys. Oceanogr.*, **16**, 856–885.

Griffin, D. A., and P. H. LeBlond, 1990: Estuary/Ocean exchange controlled by spring-neap tidal mixing. *Estuar. Coastal Shelf Sci.*, **30**, 275–297.

Gurvich, A. S., and A. M. Yaglom, 1967: Breakdown of eddies and probability distributions for small-scale turbulence. *Phys. Fluid,* **10,** S.59–65.

Holloway, G., 1988: The buoyancy flux from internal gravity wave breaking. *Dyn. Atmos. Oceans,* **12,** 107–125.

Itsweire, E. C., J. R. Koseff, D. A. Briggs, and J. H. Feiziger, 1992: Turbulance in stratified shear-flow: Implications for interpreting shear-induced mixing in the ocean. *J. Phys. Oceanogr.,* **23,** 1508–1522.

Ivey, G. N., and J. Imberger, 1991: On the nature of turbulence in a stratified fluid. Part I: The energetics of mixing. *J. Phys. Oceanogr.,* **21,** 650–658.

Jenkins, G. M., and D. G. Watts, 1968: *Spectral Analysis and its Applications.* Holden-Day, 525 pp.

Kaimal, J. C., J. C. Wyngaard, Y. Izumi, and O. R. Coté, 1972: Spectral characteristics of surface-layer turbulence. *Quart. J. Roy. Meteor. Soc.,* **98,** 563–589.

Lenschow, D. H., J. Mann, and L. Kristensen, 1994: How long is long enough when measuring fluxes and other turbulence statistics? *J. Atmos. Oceanic Technol.,* **11,** 661–673.

Linden, P. F., 1979: Mixing in stratified fluids. *Geophys. Astrophys. Fluid Dyn.,* **13,** 3–23.

Miller, P. L., 1991: Mixing in high Schmidt number turbulent jets. Ph.D. thesis, California Institute of Technology, 130 pp.

Moum, J. N., 1990: The quest for K_ρ: Preliminary results from direct measurements of turbulent fluxes in the ocean. *J. Phys. Oceanogr.,* **20,** 1980–1984.

——, 1995: Efficiency of mixing in the main thermocline. *J. Geophys. Res.,* submitted.

——, D. R. Caldwell, and C. A. Paulson, 1989: Mixing in the equatorial surface layer and thermocline. *J. Geophys. Res.,* **94**(C2), 2005–2021.

——, M. C. Gregg, R.-C. Lien, and M-E. Carr, 1995: Comparison of turbulent kinetic energy dissipation rates from two ocean microstructure profilers. *J. Atmos. Oceanic Technol.,* **11,** 346–366.

Nasmyth, P. W., 1970: Oceanic turbulence. Ph.D. thesis., University of British Columbia, 69 pp.

Ninnis, R., 1984: The effects of spatial averaging on airfoil probe measurements of oceanic velocity microstructure. Ph.D. thesis, University of British Columbia, 109 pp.

Oakey, N. S., 1982: Determination of the rate of dissipation of turbulent energy from simultaneous temperature and velocity shear microstructure measurements. *J. Phys. Oceanogr.,* **12,** 256–271.

——, 1985: Statistics of mixing parameters in the upper ocean during JASIN Phase 2. *J. Phys. Oceanogr.,* **15,** 1662–1675.

Osborn, T. R., 1980: Estimates of the local rate of vertical diffusion from dissipation measurements. *J. Phys. Oceanogr.,* **10,** 83–89.

——, and C. S. Cox, 1972: Oceanic fine structure. *Geophys. Fluid Dyn.,* **3,** 321–345.

Peters, H., M. C. Gregg, and J. M. Toole, 1988: On the parameterization of equatorial turbulence. *J. Geophys. Res.,* **93**(C2), 1199–1218.

Pond, S., J. E. Paquin, G. McBean, and R. W. Stewart, 1971: Measurements of the turbulent fluxes of momentum, moisture, and sensible heat over the ocean. *J. Atmos. Sci.,* **28,** 901–917.

Rohr, J., and C. Van Atta, 1987: Mixing efficiency in stably stratified growing turbulence. *J. Geophys. Res.,* **92**(C5), 5481–5488.

——, E. C. Itsweire, and C. W. Van Atta, 1984: Mixing efficiency in stably-stratified decaying turbulence. *Geophys. Astrophys. Fluid Dyn.,* **29,** 221–236.

Seim, H. E., and M. C. Gregg, 1994: Detailed observations of a naturally occurring shear instability. *J. Geophys. Res.,* **99** (C5), 10 049–10 073.

Shay, T. J., and M. C. Gregg, 1984: Turbulence in an oceanic convective mixed layer. *Nature,* **310,** 282–285.

Sherman, J. T., and R. E. Davis, 1995: Observations of temperature microstructure in NATRE. *J. Phys. Oceanogr.,* **9,** 1913–1929.

Simpson, J. H., and J. R. Hunter, 1974: Fronts in the Irish Sea. *Nature,* **250,** 404–406.

Stewart, R. W., 1959: The problem of diffusion in a stratified fluid. *Advances in Geophysics,* Vol. 6, Academic Press, 303–311.

Tennekes, H., and J. L. Lumley, 1972: *A First Course in Turbulence.* The MIT Press, 300 pp.

Thorpe, S. A., 1977: Turbulence and mixing in a Scottish loch. *Philos. Trans. Roy. Soc. London A,* **286,** 125–181.

Yamazaki, H., and T. Osborn, 1993: Direct estimation of heat flux in a seasonal thermocline. *J. Phys. Oceanogr.,* **23,** 503–516.